Available online at www.sciencedirect.com

SCIENCE DIRECT®

Journal of Computational Physics 207 (2005) 1–27

JOURNAL OF
COMPUTATIONAL
PHYSICS

www.elsevier.com/locate/jcp

A DLM/FD method for fluid/flexible-body interactions

Zhaosheng Yu *

Department of Applied Physics, Physics of Complex Fluids, University of Twente, P.O. Box 217, 7500 AE, Enschede, The Netherlands

Received 17 August 2004; received in revised form 20 December 2004; accepted 27 December 2004
Available online 3 March 2005

Abstract

In this study, we extended the distributed-Lagrange-multiplier/fictitious-domain (DLM/FD) formulation of Glowinski et al. [Int. J. Multiphase Flow 25 (1999) 755] for the fluid/rigid-body interactions to deal with the fluid/flexible-body interactions by replacing Newton's equations of motion for the rigid body with the continuum equations for the general solid material. Similar to the rigid-body case where the DLM is introduced as a pseudo body force to enforce the constraint of rigid-body motion of the fictitious fluid in the solid domain, the Lagrange multiplier in our formulation is to enforce the fictitious fluid to move at the same velocity as the solid. For our computational scheme, a first-order accurate fractional step scheme is employed to decouple the entire system into three sub-systems: a fluid problem, a solid problem and a Lagrange multiplier problem; the flow problem is solved with the projection method on half-staggered grids; the solid problem is solved with the Lagrangian finite element method and the Newton iterative method; and the incompressibility of the material is implemented with the penalty function method. The proposed method is applied to two typical fluid–structure interaction problems: the flow-driven oscillation of a flexible plate along the flow direction and the self-sustained oscillation across the flow direction. Both results compare favorably with previously reported numerical and experimental results, and show that our method is suited to the simulation of the motion of an incompressible non-linear elastic material in a fluid.

1. Introduction

Multiphase flows are widespread in nature and industrial applications. With the rapid development of computer power, the direct numerical simulation (DNS), based on the Navier–Stokes equations or the discrete lattice-Boltzmann equation for the solution of the fluid-flow problem, has become a practical and important tool to probe the mechanics of multiphase flows. Over the past decade a variety of DNS methods

---

* Corresponding author. Tel.: +31 53 4893093; fax: +31 53 4891096.
E-mail address: yuzhaosheng@yahoo.com.

0021-9991/$ - see front matter
doi:10.1016/j.jcp.2004.12.026

have been proposed. They can be classified into two families: boundary-fitted methods and non-boundary-fitted methods, according to whether or not the boundary-fitted mesh is used for the solution of the flow field. For the boundary-fitted methods, the fluid flow is computed on a boundary-fitted mesh, usually with the finite element method (FEM) [1–3], or the boundary element method (BEM) [4], and remeshing is required as the interfaces move (except BEM). For the non-boundary-fitted methods, the fluid flow is computed on a stationary grid and remeshing is not required. The non-boundary-fitted methods are, generally speaking, simpler and more efficient than the boundary-fitted methods, and consequently have attracted more attention, as evidenced by the emergence of a variety of such methods for multicomponent fluid flows [5–10], the fluid/rigid-solid system [11–13], and the fluid/elastic-solid problem [14–16].

When applying the non-boundary-fitted scheme to the fluid–solid system and solving the fluid-flow equation with grids extending into the interior of the solid, one actually uses the ''fictitious domain'' (FD) technique, which was initially developed to solve partial differential equations in a complex geometry. Glowinski et al. [17–20] described the FD methods for the Dirichlet problem in which the boundary condition is enforced with the Lagrange multiplier method, and they employed the methods to solve some differential equations and the incompressible viscous unsteady flows in complex or moving geometries. The Lagrange multiplier based FD method was also used by Bertrand et al. [21] and Tanguy et al. [22] to calculate the three-dimensional Stokes flows of Newtonian and visco-plastic fluids in a mixer. Glowinski et al. [12,23] developed the distributed-Lagrange-multiplier (DLM) based FD method to simulate particulate flows where the rigid particles move freely. The key idea in this method is that the interior domains of the particles are filled with the same fluids as the surroundings and the Lagrange multiplier (physically a pseudo body force) is introduced to enforce the interior (fictitious) fluids to satisfy the constraint of rigid body motion. The method has been successfully applied to the simulation of particulate flows [23–26].

In the field of fluid/flexible-body interactions, the arbitrary Lagrangian Eulerian (ALE) finite element method [3,27] is a widely used one, however, the fictitious domain method has become increasingly popular. There have existed three different FD-method-based schemes in the literature: non-body-force-based scheme, body-force-based (but non-DLM-based) scheme, and DLM-based scheme. The method used by Farnell et al. [16] for the simulation of a filament in a flowing soap film belongs to the first category, and the feature of this method is that the motion of the filament is determined by the fluid pressure force acting on the filament and then it in turn affects the fluid motion by requiring the fluid velocities at the grids inside the filament (with an assumed numerical thickness) to equal the filament velocity. The immersed boundary method proposed by Peskin [14] is a non-DLM-based FD method (as pointed out by Glowinski et al. [12]), which has been applied to a wide range of fluid–structure interaction problems (e.g. Eggleton and Popel [28], Zhu and Peskin [29]). In this method, the flexible body moves at the same velocity as the local fluid, and then affects the fluid motion through an elastic force that is calculated with the known deformation of the body and is introduced into the fluid momentum equation as a pseudo body force. For both methods, the no-slip velocity constraint is simply enforced at a fractional time step, either requiring the fluid velocity to equal the known solid velocity, or the solid velocity to equal the known fluid velocity. By contrast, in the DLM-based FD/ME method of Baaijens [15], the no-slip velocity constraint is imposed as an equation for the Lagrange multiplier defined on the solid boundary (i.e., a pseudo body force), and the fluid and solid velocities are obtained simultaneously. Another feature of Baaijens' method is that it directly solves the solid momentum and continuity equations, and consequently can account for the effect of the material physical thickness, whereas the other two schemes are suited to the problems where the material thickness is negligibly small, as a result of their simple algorithms. An important feature of the pseudo-body-force based methods including the DLM-based one is that the hydrodynamic force on the solid boundary is not required to determine the motion of the solid.

The Baaijens' method has been verified by experiment (de Hart et al. [30]) and successfully applied to the fluid–structure interaction in the aortic valve (e.g. de Hart et al. [31]). However, its formulation was derived under the assumption that the inertial effect and the real body force are not present. The aim of this work is to present a complete DLM-based FD formulation, which is a generalization of the DLM/FD formulation of Glowinski et al. [12] from the rigid-body case to the general solid material case, and differs from Baaijens' formulation in that we use the DLM to enforce the fluid to move at the same velocity as the solid not only on the solid boundary but also inside the solid domain.

Following the derivation procedure of Glowinski et al. [12], we will derive the new formulation in the following section. A simple and efficient computational scheme will be described in Section 3. We verify our method by applying it to two typical fluid–structure interaction problems in Section 4 and give the concluding remarks in the last section.

2. DLM/FD formulation

2.1. The governing equations in the strong form

The motion of the elastic body is described with the Lagrangian method. Let $P(t)$ and $\partial P(t)$ represent the solid domain and its boundary at current configuration $\mathbf{x}$, P_0 the solid domain at a reference configuration $\mathbf{X}$, Ω the entire domain comprising both interior and exterior of the body, and Γ the boundary of Ω. A schematic diagram in the 2-D case is shown in Fig. 1.

The governing equations consist of the following three parts.

1. *Fluid motion:*

$$\rho_f \frac{\mathrm{d}\mathbf{u}_f}{\mathrm{d}t} = \nabla \cdot \boldsymbol{\sigma}_f + \rho_f \mathbf{f}_f \quad \text{in } \Omega \setminus P(t), \tag{1}$$

$$\nabla \cdot \mathbf{u}_f = 0 \quad \text{in } \Omega \setminus P(t), \tag{2}$$

$$\boldsymbol{\sigma}_f = -p\mathbf{I} + 2\eta\mathbf{D} \quad \text{in } \Omega \setminus P(t), \tag{3}$$

$$\mathbf{u}_f = \mathbf{u}_\Gamma \quad \text{on } \Gamma, \tag{4}$$

$$\mathbf{u}_f = \mathbf{u}_s \quad \text{on } \partial P, \tag{5}$$

$$\mathbf{u}_f(t=0) = \mathbf{u}_{f0} \quad \text{in } \Omega \setminus P(t). \tag{6}$$

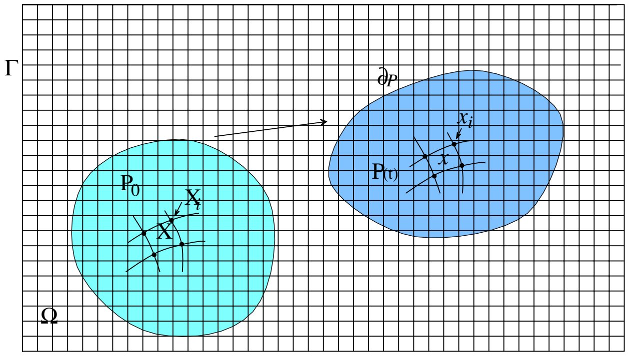

Fig. 1. The schematic diagram of the fictitious domain method for the solution of the fluid–solid system in the two-dimensional case.

2. *Solid motion:*

$$\rho_s \frac{\mathrm{d}\mathbf{u}_s}{\mathrm{d}t} = \nabla \cdot \boldsymbol{\sigma}_s + \rho_s \mathbf{f}_s \quad \text{in } P(t), \tag{7}$$

$$J\rho_s = \rho_0 \quad \text{in } P(t), \tag{8}$$

$$\boldsymbol{\sigma}_s = \frac{\lambda_0 \ln J}{J}\mathbf{I} + \frac{G}{J}(\mathbf{B} - \mathbf{I}) \quad \text{in } P(t), \tag{9}$$

$$\boldsymbol{\sigma}_s \cdot \mathbf{n} = \boldsymbol{\sigma}_f \cdot \mathbf{n} + \mathbf{f}^e \quad \text{on } \partial P, \tag{10}$$

$$\mathbf{u}_s(t=0) = \mathbf{u}_{s0} \quad \text{in } P(t). \tag{11}$$

3. *Kinematic equations:*

$$\frac{\mathrm{d}\mathbf{x}}{\mathrm{d}t} = \mathbf{u}_s \quad \text{in } P(t), \tag{12}$$

$$\mathbf{x}(t=0) = \mathbf{x}_0 \quad \text{in } P(t). \tag{13}$$

Eqs. (1)–(3) are the momentum equation, the continuity equation and the constitutive equation for a Newtonian fluid, respectively. Here, $\mathbf{u}_f$, p, ρ_f, $\mathbf{f}_f$, σ_f, $\mathbf{D}$ and $\mathbf{I}$ are the fluid velocity, pressure, density, body force, stress tensor, rate of deformation tensor, and unit tensor, respectively.

Eqs. (7)–(9) represent the momentum equation, the continuity equation and the constitutive equation for the solid motion, respectively. In (7), $\mathbf{u}_s$ denotes the solid velocity, ρ_s density, $\mathbf{f}_s$ body force, and $\boldsymbol{\sigma}_s$ Cauchy stress tensor at the current configuration $\mathbf{x}$. In (8), J is the determinant of deformation (gradient) tensor $\mathbf{F}$ and ρ_0 is the density at the reference configuration $\mathbf{X}$. $\mathbf{F}$ describes the material deformation at the current configuration with respect to the reference configuration and is defined by $\mathbf{F} = \partial\mathbf{x}/\partial\mathbf{X} \equiv (\nabla_0\mathbf{x})^{\mathrm{T}}$. Eq. (9) is the constitutive equation for the neo-Hookean material [32], in which $\mathbf{B}$ is Finger tensor, defined by $\mathbf{B} = \mathbf{F} \cdot \mathbf{F}^{\mathrm{T}}$, and λ_0, G are two material parameters characterizing the elastic solid: λ_0 is related to the compressibility property of the material and G represents the shear modulus of the material. In this study, we assume the material is incompressible, i.e., $J = 1$, but for simplicity this constraint is imposed with a penalty-function-like approximation by setting a large enough value for λ_0. An alternate way to implement the incompressibility constraint is to replace $\frac{\lambda_0 \ln J}{J}$ with the pressure $-p_s$ and then determine the pressure with equation '$J = 1$', as in Baaijens [15].

In (10), $\mathbf{n}$ is the normal unit vector on the solid surface directing inwards the fluid and $\mathbf{f}^e$ denotes the non-hydrodynamic force (density) on the solid surface such as external surface forces or contact forces between either two different bodies or between two different parts of the same (flexible) body.

For convenience of exposition, the Dirichlet boundary condition is imposed on the outer boundary Γ, as in (4), and the flexible body is suspended in the fluid so that the stress boundary condition (10) is imposed on the entire solid surface. The application of the method to be presented below, however, is not limited to these assumptions, as shown in our numerical examples.

Next, we follow the procedure of Glowinski et al. [12] to derive the FD/DLM formulation for a general solid material. The case of two-dimensions is considered.

2.2. Weak form

We define the following combined velocity space:

$$W_{\mathbf{u}} = \{(\mathbf{u}_f, \mathbf{u}_s) | \mathbf{u}_f \in H^1(\Omega \setminus P)^2,\ \mathbf{u}_s \in H^1(P)^2,\ \mathbf{u}_f = \mathbf{u}_s \quad \text{on } \partial P,\ \mathbf{u}_f = \mathbf{u}_\Gamma \quad \text{on } \Gamma\} \tag{14}$$

and corresponding combined variance space

$$W_0 = \{(\mathbf{v}_f, \mathbf{v}_s) | \mathbf{v}_f \in H^1(\Omega \setminus P)^2,\ \mathbf{v}_s \in H^1(P)^2,\ \mathbf{v}_f = \mathbf{v}_s \quad \text{on } \partial P,\ \mathbf{v}_f = 0 \quad \text{on } \Gamma\} \tag{15}$$

and perform the following symbolic operations:

$$\int_{\Omega\backslash P} \text{Eq. (1)} \cdot \mathbf{v}_f \, \mathrm{d}\mathbf{x} + \int_P \text{Eq. (7)} \cdot \mathbf{v}_s \, \mathrm{d}\mathbf{x}. \tag{16}$$

Integrating the stress-divergence terms by parts and substituting (10) into (16) yields

$$\int_{\Omega\backslash P} \left(\rho_f \frac{\mathrm{d}\mathbf{u}_f}{\mathrm{d}t} - \rho_f \mathbf{f}_f \right) \cdot \mathbf{v}_f \, \mathrm{d}\mathbf{x} + \int_{\Omega\backslash P} \boldsymbol{\sigma}_f : \nabla \mathbf{v}_f \, \mathrm{d}\mathbf{x} + \int_P \left(\rho_s \frac{\mathrm{d}\mathbf{u}_s}{\mathrm{d}t} - \rho_s \mathbf{f}_s \right) \cdot \mathbf{v}_s \, \mathrm{d}\mathbf{x} + \int_P \boldsymbol{\sigma}_s : \nabla \mathbf{v}_s \, \mathrm{d}\mathbf{x}$$
$$= \int_{\partial P} \mathbf{f}^e \cdot \mathbf{v}_s \, \mathrm{d}\mathbf{x} \quad \text{for all } (\mathbf{v}_f, \mathbf{v}_s) \in W_0. \tag{17}$$

It is not surprising that the hydrodynamic forces on the solid boundary cancel in the combined momentum equation (17), since they represent *internal* forces for the combined fluid–solid system [12].

2.3. FD weak formulation

To construct a fictitious domain formulation, we extend the fluid computational domain from $\Omega\backslash P$ to Ω, and couple the velocities $\mathbf{u}_f$ and $\mathbf{u}_s$ not only via the solid surface ∂P, but the entire solid domain P. The combined velocity and variance spaces are modified as follows:

$$\widetilde{W}_{\mathbf{u}} = \{(\mathbf{u}_f, \mathbf{u}_s) | \mathbf{u}_f \in H^1(\Omega)^2,\ \mathbf{u}_s \in H^1(P)^2,\ \mathbf{u}_f = \mathbf{u}_s \quad \text{in } P,\ \mathbf{u}_f = \mathbf{u}_\Gamma \quad \text{on } \Gamma\}, \tag{18}$$

$$\widetilde{W}_0 = \{(\mathbf{v}_f, \mathbf{v}_s) | \mathbf{v}_f \in H^1(\Omega)^2,\ \mathbf{v}_s \in H^1(P)^2,\ \mathbf{v}_f = \mathbf{v}_s \quad \text{in } P,\ \mathbf{v}_f = 0 \quad \text{on } \Gamma\}. \tag{19}$$

Noting that

$$\int_P \left(\rho_f \frac{\mathrm{d}\mathbf{u}_f}{\mathrm{d}t} - \rho_f \mathbf{f}_f \right) \cdot (\mathbf{v}_f - \mathbf{v}_s) \, \mathrm{d}\mathbf{x} + \int_P \boldsymbol{\sigma}_f : \nabla(\mathbf{v}_f - \mathbf{v}_s) = 0 \quad \text{for all } (\mathbf{v}_f, \mathbf{v}_s) \in \widetilde{W}_0 \tag{20}$$

and adding (20) to (17), we obtain the following formulation for $(\mathbf{u}_f, \mathbf{u}_s) \in \widetilde{W}_{\mathbf{u}}$:

$$\int_\Omega \left(\rho_f \frac{\mathrm{d}\mathbf{u}_f}{\mathrm{d}t} - \rho_f \mathbf{f}_f \right) \cdot \mathbf{v}_f \, \mathrm{d}\mathbf{x} + \int_\Omega \boldsymbol{\sigma}_f : \nabla \mathbf{v}_f \, \mathrm{d}\mathbf{x} + \int_P \left[(\rho_s - \rho_f) \frac{\mathrm{d}\mathbf{u}_s}{\mathrm{d}t} - (\rho_s \mathbf{f}_s - \rho_f \mathbf{f}_f) \right] \cdot \mathbf{v}_s \, \mathrm{d}\mathbf{x}$$
$$+ \int_P (\sigma_s - \sigma_f) : \nabla \mathbf{v}_s \, \mathrm{d}\mathbf{x} = \int_{\partial P} \mathbf{f}^e \cdot \mathbf{v}_s \, \mathrm{d}\mathbf{x} \quad \text{for all } (\mathbf{v}_f, \mathbf{v}_s) \in \widetilde{W}_0. \tag{21}$$

The fluid constitutive equation can be trivially extended into the interior of the solid since (20) holds for any forms of $\boldsymbol{\sigma}_f$ in P. The fluid continuity equation (2) can also be extended into P because we consider the incompressible solid material. Even if the solid material is not exactly incompressible (but nearly incompressible), we believe that this extension is acceptable, since the solid continuity equation is based on the deformation history, and for J being close to unity, the divergence-free approximation for the instantaneous velocity should be good enough.

The space for the fluid pressure in Ω can be defined as

$$L_0^2(\Omega) = \left\{ p \in L^2(\Omega) \middle| \int_\Omega p \, \mathrm{d}\mathbf{x} = 0 \right\}. \tag{22}$$

The weak form of the fluid continuity equation in Ω is

$$\int_\Omega q\nabla\cdot\mathbf{u}_f\,\mathrm{d}\mathbf{x}=0\quad\text{for all } q\in L^2(\Omega).\tag{23}$$

Since '$J = 1$' is enforced with the penalty-function method, the combined momentum equation (21) with the stresses substituted from the constitutive equations (3) and (9), the fluid continuity equation (23), the kinematic equation (12), and together with the initial conditions (6), (11) and (13), form a complete set of FD based governing equations.

2.4. DLM/FD weak formulation

Finally, the DLM is introduced to relax the constraints '$\mathbf{u}_f = \mathbf{u}_s$ in P' from the combined velocity space and the corresponding constraint from the combined variance space, resulting in the following DLM/FD based momentum equations from (21) for $\mathbf{u}_f\in\overline{W}_\mathbf{u}$, $\mathbf{u}_s\in H^1(P)^2$ and $\boldsymbol{\lambda}\in\Lambda$:

$$\int_\Omega\left(\rho_f\frac{\mathrm{d}\mathbf{u}_f}{\mathrm{d}t}-\rho_f\mathbf{f}_f\right)\cdot\mathbf{v}_f\,\mathrm{d}\mathbf{x}+\int_\Omega\boldsymbol{\sigma}_f:\nabla\mathbf{v}_f\,\mathrm{d}\mathbf{x}=\langle\boldsymbol{\lambda},\mathbf{v}_f\rangle_P\quad\text{for all }\mathbf{v}_f\in\overline{W}_0,\tag{24}$$

$$\begin{aligned}&\int_P\left[(\rho_s-\rho_f)\frac{\mathrm{d}\mathbf{u}_s}{\mathrm{d}t}-(\rho_s\mathbf{f}_s-\rho_f\mathbf{f}_f)\right]\cdot\mathbf{v}_s\,\mathrm{d}\mathbf{x}+\int_P(\boldsymbol{\sigma}_\mathbf{s}-\boldsymbol{\sigma}_f):\nabla\mathbf{v}_s\,\mathrm{d}\mathbf{x}\\&\quad=\int_{\partial P}\mathbf{f}^e\cdot\mathbf{v}_s\,\mathrm{d}\mathbf{x}-\langle\boldsymbol{\lambda},\mathbf{v}_s\rangle_P\quad\text{for all }\mathbf{v}_s\in H^1(P)^2,\end{aligned}\tag{25}$$

$$\langle\mathbf{u}_f-\mathbf{u}_s,\boldsymbol{\zeta}\rangle_P=\mathbf{0}\quad\text{for all }\boldsymbol{\zeta}\in\Lambda,\tag{26}$$

where $\boldsymbol{\lambda}$ and $\boldsymbol{\zeta}$ are the DLM and its variance defined in the space Λ, respectively, $\langle\cdot,\cdot\rangle_P$ denotes an appropriate inner product, and:

$$\overline{W}_\mathbf{u}=\{\mathbf{u}_f|\mathbf{u}_f\in H^1(\Omega)^2,\ \mathbf{u}_f=\mathbf{u}_\Gamma\quad\text{on }\Gamma\},\tag{27}$$

$$\overline{W}_0=\{\mathbf{v}_f|\mathbf{v}_f\in H^1(\Omega)^2,\ \mathbf{v}_f=0\quad\text{on }\Gamma\}.\tag{28}$$

A variety of choices of the definitions of the multiplier space Λ and the inner product $\langle\cdot,\cdot\rangle_P$ are possible, such as $H^1(P)^2$ and $L^2(P)^2$ for Λ, and the corresponding standard inner products for $\langle\cdot,\cdot\rangle_P$, respectively [12]. To our knowledge, the former choice, however, has never been implemented numerically in the previous works for the rigid-body problems, presumably due to the implementation difficulty arising from the use of two different sets of meshes for the velocity and the Lagrange multiplier. For its simplicity, the collocation point method has been widely used [12,21,24], which makes sense only for the discrete space. In this method, the discrete multiplier space is characterized by Dirac delta functions at points covering uniformly the solid domain, and $\langle\cdot,\cdot\rangle_P$ is defined as the discrete L^2 inner product [12].

In the present study, we use a collocation-point-like scheme, which is resulted from the choices of the L^2 inner product for $\langle\cdot,\cdot\rangle_P$, $H^1(P)^2$ for Λ, and then the application of the trapezoidal rule to the integration in the finite-element discretization. The method differs from the collocation point method only in that the discrete L^2 inner product between the velocity and the multiplier (or their variances) is weighted with the support areas of the shape functions for the points (or nodes). It should be noted that the application of the trapezoidal rule not only simplifies the computation, but also improves the stability of the algorithm, since we found that the computation with the collocation-point-like scheme was stable, whereas the one with the Gaussian rule instead for the integration was not. One anonymous referee of the current paper argued that the formulation (24)–(26) with the above choices of the multiplier space and the inner product is ill-posed due to the fact that the normal derivatives of the exact solution of the velocity overcome a jump through the solid boundary. The argument is true, but our definition of the multiplier space Λ as $H^1(P)^2$ only has a nominal sense, and using the collocation-point-like method, we actually do not seek the solution of the Lagrange multiplier in $H^1(P)^2$. In the formulations below, we will substitute the L^2 inner product for $\langle \cdot , \cdot \rangle_P$, but retain the exposition of the multiplier space as Λ to avoid confusion. The collocation-point-like method used here may not be the best one and further investigation on the choices of the multiplier space and the inner product is our future work.

When $\langle \cdot , \cdot \rangle_P$ is defined as the L^2 inner product, the Lagrange multiplier $\boldsymbol{\lambda}$ can be directly interpreted as a pseudo body force on the fictitious fluid in the solid domain, enforcing the inner fluid to move at the same velocity as the solid, as can be seen from (24) and (26). This physical implication in the DLM/FD formulation has been made clear by Glowinski et al. [12] in their work on the rigid body where the Lagrange multiplier (i.e., pseudo body force) is required to maintain the rigid-body motion of the fictitious fluid. The DLM $\boldsymbol{\lambda}$ is analogous to the pressure in incompressible fluid flows, whose gradient is the (pseudo body) force required to maintain the constraint of incompressibility, as pointed out by Glowinski et al. [12]. It is well known that the pressure can be also mathematically interpreted as a Lagrange multiplier.

We wish to make some comments on the differences between our formulation and other formulations including Baaijens' and Peskin's. As already mentioned in the introduction, the feature of Baaijens' formulation is that the Lagrange multiplier is defined on the surface of the body. Since the FD formulation with the surface multiplier does not impose any constraint to the fluid velocity inside the solid body, the extension condition (20) for obtaining a FD formulation cannot rigorously hold, and hence, the application of the formulation is limited to the cases where the extension of the fluid equations into the solid domain does not introduce significant errors. The Peskin's formulation differs from ours in that an elastic body force rather than a Lagrange multiplier is introduced into the fluid equation and that the strong form rather than the weak form is directly used. The strong form of our formulation is essentially same as his, and the only difference lies in an unimportant term $\int_P \boldsymbol{\sigma}_f : \nabla \mathbf{v}_s \, \mathrm{d}\mathbf{x}$. We inspected the effect of the term $\int_P \boldsymbol{\sigma}_f : \nabla \mathbf{v}_s \, \mathrm{d}\mathbf{x}$ on the motion of the leaflet in our first numerical example below, and found that its effect was indeed negligible, which is not surprising since the rate of deformation of the solid material is normally very small.

Our formulation is a straightforward extension of the DLM/FD formulation of Glowinski et al. [12] from the rigid-body case to the general solid material case by replacing Newton's equations of motion with the continuum equations. By imposing the rigid-body motion constraints to the velocity and its variance in the solid domain, we find that our formulation reduces to theirs.

2.4.1. Governing equations for Newtonian fluid and neo-Hookean solid

Now we consider the special cases where gravity is the only real body force for both the fluid and the solid, and the non-hydrodynamic force on the solid surface is absent. The formulation for the incompressible neo-Hookean material immersed in a Newtonian fluid with the penalty function approximation is stated as follows:

find $\mathbf{u}_f \in \overline{W}_{\mathbf{u}}$, $p \in L_0^2(\Omega)$, $\mathbf{u}_s \in H^1(P)^2$ and $\boldsymbol{\lambda} \in \Lambda$ satisfying

$$\int_\Omega \rho_f \left(\frac{\partial \mathbf{u}_f}{\partial t} + \mathbf{u}_f \cdot \nabla \mathbf{u}_f \right) \cdot \mathbf{v}_f \, \mathrm{d}\mathbf{x} + \int_\Omega \left(-p\mathbf{I} + \eta (\nabla \mathbf{u}_f)^{\mathrm{T}} \right) : \nabla \mathbf{v}_f \, \mathrm{d}\mathbf{x} = \int_P \boldsymbol{\lambda} \cdot \mathbf{v}_f \, \mathrm{d}\mathbf{x} \quad \text{for all } \mathbf{v}_f \in \overline{W}_0, \tag{29}$$

$$\int_\Omega q \nabla \cdot \mathbf{u}_f \, \mathrm{d}\mathbf{x} = \mathbf{0} \quad \text{for all } q \in L^2(\Omega), \tag{30}$$

$$\begin{aligned} &\int_P \left[(\rho_s - \rho_f) \left(\frac{\mathrm{d}\mathbf{u}_s}{\mathrm{d}t} - \mathbf{g} \right) \right] \cdot \mathbf{v}_s \, \mathrm{d}\mathbf{x} + \int_P (\nabla \mathbf{v}_s)^{\mathrm{T}} : [\lambda_0 \ln J \mathbf{I} + G(\mathbf{B} - \mathbf{I})] \, \mathrm{d}\mathbf{x} \\ &\quad - \int_P (\nabla \mathbf{v}_s)^{\mathrm{T}} : \{ -p\mathbf{I} + \eta [\nabla \mathbf{u}_f + (\nabla \mathbf{u}_f)^{\mathrm{T}}] \} \, \mathrm{d}\mathbf{x} = - \int_P \boldsymbol{\lambda} \cdot \mathbf{v}_s \, \mathrm{d}\mathbf{x} \quad \text{for all } \mathbf{v}_s \in H^1(P)^2, \end{aligned} \tag{31}$$

$$\int_P (\mathbf{u}_f - \mathbf{u}_s)\cdot\boldsymbol{\zeta}\,\mathrm{d}\mathbf{x} = \mathbf{0} \quad \text{for all } \boldsymbol{\zeta}\in\Lambda, \tag{32}$$

as well as the kinematic equation (12), and the initial conditions (6), (11) and (13). The gravity term in the fluid momentum equation (29) is dropped, which means the hydrostatic pressure is not included in the computed fluid pressure.

2.4.2. Dimensionless governing equations

Eqs. (29)–(32) can be non-dimensionlized by introducing the following scales: L_c for length, U_c for velocity, L_c/U_c for time, $\rho_f U_c^2$ for the pressure p and parameters λ_0 and G, and $\rho_f U_c^2/L_c$ for the Lagrange multiplier. For convenience, we write the dimensionless quantities in the same form as their dimensional counterparts, unless otherwise specified. Then (29)–(32) become, respectively:

$$\int_\Omega \left(\frac{\partial \mathbf{u}_f}{\partial t} + \mathbf{u}_f\cdot\nabla\mathbf{u}_f\right)\cdot\mathbf{v}_f\,\mathrm{d}\mathbf{x} + \int_\Omega \left(-p\mathbf{I} + \frac{1}{Re}(\nabla\mathbf{u}_f)^{\mathrm{T}}\right) : \nabla\mathbf{v}_f\,\mathrm{d}\mathbf{x} = \int_P \boldsymbol{\lambda}\cdot\mathbf{v}_f\,\mathrm{d}\mathbf{x}, \tag{33}$$

$$\int_\Omega q\nabla\cdot\mathbf{u}_f\,\mathrm{d}\mathbf{x} = 0, \tag{34}$$

$$\begin{aligned}&\int_P \left[(\rho_r - 1)\left(\frac{\mathrm{d}\mathbf{u}_s}{\mathrm{d}t} - Fr\frac{\mathbf{g}}{g}\right)\right]\cdot\mathbf{v}_s\,\mathrm{d}\mathbf{x} + \int_P (\nabla\mathbf{v}_s)^{\mathrm{T}} : [\bar{\lambda}_0 \ln J\mathbf{I} + \overline{G}(\mathbf{B}-\mathbf{I})]\,\mathrm{d}\mathbf{x}\\ &\quad - \int_P (\nabla\mathbf{v}_s)^{\mathrm{T}} : \left\{-p\mathbf{I} + \frac{1}{Re}[\nabla\mathbf{v}_f + (\nabla\mathbf{v}_f)^{\mathrm{T}}]\right\}\mathrm{d}\mathbf{x} = -\int_P \boldsymbol{\lambda}\cdot\mathbf{v}_s\,\mathrm{d}\mathbf{x},\end{aligned} \tag{35}$$

$$\int_P (\mathbf{u}_f - \mathbf{u}_s)\cdot\boldsymbol{\zeta}\,\mathrm{d}\mathbf{x} = \mathbf{0}, \tag{36}$$

in which the following dimensionless parameters are introduced:

$$\text{density ratio:} \quad \rho_r = \rho_s/\rho_f, \tag{37}$$

$$\text{material parameters:} \quad \bar{\lambda}_0 = \lambda_0/\rho_f U_c^2, \overline{G} = G/\rho_f U_c^2, \tag{38}$$

$$\text{Reynolds number:} \quad Re = \frac{\rho_f U_c L_c}{\eta}, \tag{39}$$

$$\text{Froude number:} \quad Fr = \frac{gL_c}{U_c^2}. \tag{40}$$

Here, the Froude number represents the relative importance of gravity with respect to inertia.

3. Computational scheme

The motion of an elastic body is solved from the Lagrangian formulation, in which the integration of the Lagrangian variables can be performed at either **X** or **x**. We choose **X** here because in the elastic stress term a derivative of the shape function with respect to the configuration is required, while the current configuration **x** is unknown. We take the configuration **x** as an independent variable, instead of the solid velocity, and define the DLM in the Lagrangian frame. Noting that $(\nabla\mathbf{v}_s)^{\mathrm{T}} = (\nabla_0\mathbf{v}_s)^{\mathrm{T}}\cdot\mathbf{F}^{-1}$, Eqs. (33)–(36) become:

find $\mathbf{u}_f \in \overline{W}_{\mathbf{u}}$, $p \in L_0^2(\Omega)$, $\mathbf{x} \in H^1(P_0)^2$ and $\boldsymbol{\lambda} \in \Lambda$ satisfying

$$\int_\Omega \left(\frac{\partial \mathbf{u}_f}{\partial t} + \mathbf{u}_f \cdot \nabla \mathbf{u}_f\right) \cdot \mathbf{v}_f \,\mathrm{d}\mathbf{x} + \int_\Omega \left(-p\mathbf{I} + \frac{1}{Re}(\nabla \mathbf{u}_f)^{\mathrm{T}}\right) : \nabla \mathbf{v}_f \,\mathrm{d}\mathbf{x} = \int_{P_0} \boldsymbol{\lambda} \cdot \mathbf{v}_f \,\mathrm{d}\mathbf{X} \quad \text{for all } \mathbf{v}_f \in \overline{W}_0, \tag{41}$$

$$\int_\Omega q \nabla \cdot \mathbf{u}_f \,\mathrm{d}\mathbf{x} = \mathbf{0} \quad \text{for all } q \in L^2(\Omega), \tag{42}$$

$$\begin{aligned}\int_{P_0} \left[(\rho_r - 1)\left(\frac{\mathrm{d}^2\mathbf{x}}{\mathrm{d}t^2} - Fr\frac{\mathbf{g}}{g}\right)\right] \cdot \mathbf{v}_s \,\mathrm{d}\mathbf{X} + \int_{P_0} (\nabla_0 \mathbf{v}_s)^{\mathrm{T}} : [\bar{\lambda}_0 \ln J\mathbf{F}^{-1} + \overline{G}(\mathbf{F}^{\mathrm{T}} - \mathbf{F}^{-1})] \,\mathrm{d}\mathbf{X} \\ - \int_{P_0} (\nabla_0 \mathbf{v}_s)^{\mathrm{T}} : \mathbf{F}^{-1} \cdot \left\{-p\mathbf{I} + \frac{1}{Re}\left[\nabla \mathbf{u}_f + (\nabla \mathbf{u}_f)^{\mathrm{T}}\right]\right\} \mathrm{d}\mathbf{X} = -\int_{P_0} \boldsymbol{\lambda} \cdot \mathbf{v}_s \,\mathrm{d}\mathbf{X} \quad \text{for all } \mathbf{v}_s \in H^1(P_0)^2,\end{aligned} \tag{43}$$

$$\int_{P_0} \left(\mathbf{u}_f - \frac{\mathrm{d}\mathbf{x}}{\mathrm{d}t}\right) \cdot \boldsymbol{\zeta} \,\mathrm{d}\mathbf{X} = \mathbf{0} \quad \text{for all } \boldsymbol{\zeta} \in \Lambda, \tag{44}$$

where we still use $\mathbf{v}_s$ to represent the variance of the configuration. In the above equations, all updated Lagrangian integration domains P have been transformed to P_0, however, for those terms also involving Eulerian variables, the updated configuration is still required to interpolate the Eulerian variables into the Lagrangian frame.

3.1. Fractional step scheme

The most accurate time discretization scheme is a fully coupled scheme such as the one used by Baaijens [15] where the backward Euler scheme is used to discretize the governing equations in time and the resulting non-linear algebraic equations are solved via Newton iteration. The scheme also has an advantage of high stability, but has an disadvantage of low efficiency. In this work, we attempt to devise a simple and efficient computational scheme with less emphasis on accuracy. Therefore, following the idea of Glowinski et al. [12], we employ the first-order accurate fractional step (or operator-splitting) scheme to decouple the system (41)–(44). In the immersed boundary method, the elastic force is calculated explicitly, and consequently the method is very efficient. Unfortunately, we were unable to find a robust scheme that is based on the explicit calculation of the elastic force, probably due to the different material constitutive model used here.

For convenience, we denote the elastic force term by

$$\mathbf{E} = \int_{P_0} (\nabla_0 \mathbf{v}_s)^{\mathrm{T}} : [\bar{\lambda}_0 \ln J\mathbf{F}^{-1} + \overline{G}(\mathbf{F}^{\mathrm{T}} - \mathbf{F}^{-1})] \,\mathrm{d}\mathbf{X}. \tag{45}$$

Two schemes are recommended in this study.

Scheme 1. System (41)–(44) is decoupled into three sub-problems.

Fluid problem for $\mathbf{u}_f^*$ and p

$$\begin{aligned}&\int_\Omega \left(\frac{\mathbf{u}_f^* - \mathbf{u}_f^n}{\Delta t} + \mathbf{u}_f^n \cdot \nabla \mathbf{u}_f^n\right) \cdot \mathbf{v}_f \,\mathrm{d}\mathbf{x} + \int_\Omega \left(-p\mathbf{I} + \frac{1}{Re}(\nabla \mathbf{u}_f^*)^{\mathrm{T}}\right) : \nabla \mathbf{v}_f \,\mathrm{d}\mathbf{x} = \int_{P^n} \boldsymbol{\lambda}^n \cdot \mathbf{v}_f \,\mathrm{d}\mathbf{x}^n, \\ &\int_\Omega q \nabla \cdot \mathbf{u}_f^* \,\mathrm{d}\mathbf{x} = \mathbf{0}.\end{aligned} \tag{46}$$

Solid problem for $\mathbf{x}^{n+1}$:

$$\int_{P_0}\left[(\rho_r-1)\left(\frac{\mathbf{x}^{n+1}-2\mathbf{x}^n+\mathbf{x}^{n-1}}{\Delta t^2}-Fr\frac{\mathbf{g}}{g}\right)\right]\cdot\mathbf{v}_s\,\mathrm{d}\mathbf{X}+\mathbf{E}^{n+1}-\int_{P_0}(\nabla_0\mathbf{v}_s)^{\mathrm{T}}:[(\mathbf{F}^n)^{-1}\cdot\boldsymbol{\sigma}_f^*(\mathbf{x}^n)]\,\mathrm{d}\mathbf{X}=-\int_{P^n}\boldsymbol{\lambda}^n\cdot\mathbf{v}_s\,\mathrm{d}\mathbf{x}^n. \tag{47}$$

Lagrange multiplier problem for $\mathbf{u}_f^{n+1}$ and $\boldsymbol{\lambda}^{n+1}$:

$$\int_{\Omega}\left(\frac{\mathbf{u}_f^{n+1}-\mathbf{u}_f^*}{\Delta t}\right)\cdot\mathbf{v}_f\,\mathrm{d}\mathbf{x}=\int_{P^n}(\boldsymbol{\lambda}^{n+1}-\boldsymbol{\lambda}^n)\cdot\mathbf{v}_f\,\mathrm{d}\mathbf{x}^n, \tag{48}$$

$$\int_{P^n}\left[\mathbf{u}_f^{n+1}-\frac{\mathbf{x}^{n+1}-\mathbf{x}^n}{\Delta t}\right]\cdot\boldsymbol{\zeta}\,\mathrm{d}\mathbf{x}^n=\mathbf{0}. \tag{49}$$

In (48), the superscript '*' in $\boldsymbol{\sigma}_f^*$ means that the fluid stress is calculated with $\mathbf{u}_f^*$, instead of $\mathbf{u}_f^n$, for the convenience of coding. Note that the integral of the fluid stress at $\mathbf{X}$ is transformed from the one at $\mathbf{x}^n$, and therefore the fluid stress at $\mathbf{x}^n$ rather than at $\mathbf{X}$ is used for the integration.

One can drop the Lagrange multiplier terms at the n time level in (46) and (48) from the operator-splitting scheme, and the resulting scheme has been widely used in the DLM/FD method for rigid body problems and is capable of giving reasonably accurate solutions [12,23–25]. However, we have recently found that the new scheme alone can significantly improve the accuracy of the solution for the rigid-body problems at low Reynolds numbers, in the sense that, unlike the old scheme, the new scheme does not require a very small time step to obtain a reasonably accurate solution. In addition, it is clear that the splitting error for the new scheme would vanish when steady-state is achieved.

Scheme 2. For the Lagrange multiplier problem (48) and (49), Glowinski et al. [23] obtained the analytical solution for the rigid-body case by assuming that the Lagrange multiplier does not change the velocity outside the solid boundary in this sub-problem. In fact, if we consider the velocities $\mathbf{u}_f^{n+1}$ and $\mathbf{u}_f^*$ in (48) as functions in a continuous space (not a discretized space), this assumption holds exactly. Extending the integration domain from P^n to Ω for the right-hand term of (48) by setting zero-value to the Lagrange multiplier outside P^n, we have the strong form of (48):

$$\left.\left(\frac{\mathbf{u}_f^{n+1}-\mathbf{u}_f^*}{\Delta t}\right)\right|_{P^n}=(\boldsymbol{\lambda}^{n+1}-\boldsymbol{\lambda}^n)|_{P^n}, \tag{50}$$

and $(\mathbf{u}_f^{n+1}-\mathbf{u}_f^*)|_{\Omega\backslash P^n}=0$. The strong form of (49) is

$$\left.\left(\mathbf{u}_f^{n+1}-\frac{\mathbf{x}^{n+1}-\mathbf{x}^n}{\Delta t}\right)\right|_{P^n}=0. \tag{51}$$

Substituting $\mathbf{u}_f^{n+1}$ into (50) from (51), we get a weak form of the resulting equation as follows:

$$\int_{P^n}\left(\frac{\mathbf{x}^{n+1}-\mathbf{x}^n}{\Delta t^2}-\frac{\mathbf{u}_f^*}{\Delta t}\right)\cdot\mathbf{v}_s\,\mathrm{d}\mathbf{x}^n=\int_{P^n}(\boldsymbol{\lambda}^{n+1}-\boldsymbol{\lambda}^n)\cdot\mathbf{v}_s\,\mathrm{d}\mathbf{x}^n, \tag{52}$$

which for the incompressible solid material, takes the form

$$\int_{P_0}\left(\frac{\mathbf{x}^{n+1}-\mathbf{x}^n}{\Delta t^2}-\frac{\mathbf{u}_f^*(\mathbf{x}^n)}{\Delta t}\right)\cdot\mathbf{v}_s\,\mathrm{d}\mathbf{X}=\int_{P^n}(\boldsymbol{\lambda}^{n+1}-\boldsymbol{\lambda}^n)\cdot\mathbf{v}_s\,\mathrm{d}\mathbf{x}^n. \tag{53}$$

Changing λ^n in (47) into λ^{n+1} and adding (53) to the modified solid equation, we get

$$\mathbf{E}^{n+1}+\int_{P_0}\frac{\rho_r\mathbf{x}^{n+1}}{\Delta t^2}\cdot\mathbf{v}_s\,\mathrm{d}\mathbf{X}=\int_{P_0}\left[\frac{\rho_r\mathbf{x}^n}{\Delta t^2}+\frac{\mathbf{u}_f^*(\mathbf{x}^n)}{\Delta t}+(\rho_r-1)\left(\frac{\mathbf{x}^n-\mathbf{x}^{n-1}}{\Delta t^2}+Fr\frac{\mathbf{g}}{g}\right)\right]\cdot\mathbf{v}_s\,\mathrm{d}\mathbf{X}$$
$$+\int_{P_0}(\nabla_0\mathbf{v}_s)^{\mathrm{T}}:[(\mathbf{F}^n)^{-1}\cdot\boldsymbol{\sigma}_f^*(\mathbf{x}^n)]\,\mathrm{d}\mathbf{X}-\int_{P^n}\boldsymbol{\lambda}^n\cdot\mathbf{v}_s\,\mathrm{d}\mathbf{x}^n. \quad (54)$$

Replacing the solid equation (47) with (54) and remaining the other two sub-problems in Scheme 1 results in our Scheme 2. Although, the transformations between the strong form and the weak form in (48)–(52) hold theoretically, numerical approximations are introduced in these operations, in the sense that the numerical solutions to the strong form and the weak form can not be exactly the same. However, our numerical experiments show that the two schemes produce almost the same results, indicating that the above approximations do not introduce appreciable numerical errors and Scheme 2 is as accurate as Scheme 1. We found one advantage of Scheme 2 over Scheme 1 in that for the neutrally buoyant case (i.e., $\rho_r = 1$) it is difficult, if not possible, for Scheme 1 to obtain a stable solution, whereas, Scheme 2 is stable. The most probable reason is that the presence of mass matrix for the neutrally buoyant case in (54) for Scheme 2 improves the matrix condition number. As a result, we use Scheme 2 to do calculations in this study, unless otherwise specified.

It should be noted that the above fractional step schemes are not applicable to the Stokes flow where the Reynolds number is zero, in which case one may need to seek an efficient iterative scheme.

3.2. Solution of the fluid problem

With the fictitious domain method, the fluid problem can be always posed on a regular domain and thereby solved with a structured grid system. As in [25], we use the half-staggered finite difference scheme and the projection method solve the fluid problem (46). In the half-staggered finite difference scheme, the velocity-components are co-located and the pressure nodes are staggered with the velocity nodes. Such an arrangement of the velocity and pressure nodes is a reminiscence of the "$Q_1 - P_0$" finite element scheme [33] where the velocity is piecewise bi-linear and the pressure is piecewise constant on each element. In fact, both schemes give the same spatial discretization results for the velocity diffusion term and the pressure term in the fluid momentum equation. However, since we use the projection method, the entire computational scheme is different from "$Q_1 - P_0$" finite element scheme where the velocity and the pressure are coupled.

We employ the following first-order accurate projection scheme (assume Dirichlet boundary condition; see [34] for more discussions on the projection scheme):

$$1.\quad \frac{\mathbf{u}_f^{\#}-\mathbf{u}_f^n}{\Delta t}+(\mathbf{u}_f\cdot\nabla u_f)^n=\frac{1}{Re}\nabla^2\mathbf{u}_f^{\#}-\nabla p^n+\boldsymbol{\lambda}_P^n,\qquad \mathbf{u}_f^{\#}=\mathbf{u}_\Gamma\quad\text{on }\Gamma. \quad (55)$$

$$2.\quad \nabla^2\phi=\frac{\nabla\cdot\mathbf{u}_f^{\#}}{\Delta t},\qquad \frac{\partial\phi}{\partial n}=0\quad\text{on }\Gamma. \quad (56)$$

$$3.\quad \frac{\mathbf{u}_f^*-\mathbf{u}_f^{\#}}{\Delta t}=-\nabla\phi, \quad (57)$$

$$p^{n+1}=p^n+\phi. \quad (58)$$

In (55), $\boldsymbol{\lambda}_P^n$ represents

$$\boldsymbol{\lambda}_P^n = \frac{1}{h^2} \int_{P^n} \boldsymbol{\lambda}^n \cdot \mathbf{v}_f \, \mathrm{d}\mathbf{x}^n, \tag{59}$$

where h denotes the fluid mesh, and $\mathbf{v}_f$ now represents the bi-linear shape function for the fluid nodes. The coefficient $1/h^2$ stems from the diagonal mass matrix $h^2\mathbf{I}$ of the finite element scheme for all inner fluid nodes (the nodes on the symmetrical or periodic boundary can be regarded as inner nodes by the consideration of the extended elements); the mass matrix for the finite difference scheme can be regarded as $\mathbf{I}$. The trapezoidal rule is used to integrate (59).

Eq. (55) is a diffusion problem and can be further decomposed into two tri-diagonal systems with the ADI technique. We adopt the following version [35]:

$$\begin{aligned} \frac{\mathbf{u}_f^{n+1/2} - \mathbf{u}_f^n}{\Delta t/2} &= \frac{1}{Re}\left(\nabla_x^2 \mathbf{u}_f^{n+1/2} + \nabla_y^2 \mathbf{u}_f^n\right) + \boldsymbol{\lambda}_P^n - \nabla p^n - (\mathbf{u}_f \cdot \nabla \mathbf{u}_f)^n, \\ \frac{\mathbf{u}_f^{\#} - \mathbf{u}_f^{n+1/2}}{\Delta t/2} &= \frac{1}{Re}\left(\nabla_x^2 \mathbf{u}_f^{n+1/2} + \nabla_y^2 \mathbf{u}_f^{\#}\right) + \boldsymbol{\lambda}_P^n - \nabla p^n - (\mathbf{u}_f \cdot \nabla \mathbf{u}_f)^{n+1/2}. \end{aligned} \tag{60}$$

Eq. (56) is an elliptic problem on staggered grids with a homogeneous Neumann boundary condition and can be efficiently solved by using a combination of a specialized fast cosine transformation (FCT) and a tri-diagonal system solver. The reader can find the codes of both FCT and a tri-diagonal system solver in Press et al. [36]. It is better to perform FCT in a direction with the fewer number of grids, since the computational cost of FCT is $O(N \log N)$ whereas only $O(N)$ for the tri-diagonal system solver, here N being the number of the grids in one direction.

3.3. Solution of the solid problem

We use the four-node quadrilateral element (i.e., continuous bi-linear interpolant) for both the solid configuration and the Lagrange multiplier. In (47) and (54), the penalty function term is integrated using Gaussian rule with only one Gaussian point, and all other terms except the Lagrange multiplier term are integrated with four Gaussian points (2×2). The Lagrange multiplier term is integrated using the trapezoidal rule. The fluid velocities at the Lagrangian nodes (not Gaussian points directly in this study) are obtained from the fluid nodes with the bi-linear interpolation. The implication of "$Q_1 - P_0$" element is used for determining the fluid stress at Lagrangian nodes in (54), i.e., the fluid velocity is bi-linear and the pressure is piecewise constant on each fluid element. The resulting non-linear equation (54) is solved with Newton iterations and the linearized equation in each iteration is solved with the LU decomposition method based on the implicit partial pivoting [36].

The use of the first-order accurate time scheme requires a small time step, within which the configuration change of the solid is small; as a result, the configuration obtained at a previous time level provides an excellent guess solution in the Newton iterative procedure, and we observed that it requires only 2–3 iterations to render the relative difference between the solutions at two consecutive iterations less than 10^{-6}.

3.4. Solution of the Lagrange multiplier problem

The trapezoidal rule is used to integrate all terms in (48) and (49), resulting in a collocation-point-like method to enforce the constraint of the solid and fluid velocities in the solid domain being equal, for the bi-linear Lagrange multiplier shape function used. Application of the 2×2 Gaussian integration rule to the Lagrange multiplier (and its shape function) terms was found to result in an unstable scheme, and the scheme from the use of the piece-wise constant interpolant for the Lagrange multiplier was also not as stable as the collocation-point-like method above. For consistency (in terms of the multiplier discrete space), the Lagrange multiplier terms in both fluid and solid sub-problems are also integrated with the trapezoidal rule, as mentioned earlier.

System (48) and (49) is a saddle-point problem and can be efficiently solved with the conjugate gradient iterative method (Glowinski et al. [12]). Glowinski et al. suggested the solid (or Lagrange multiplier) mesh size h_s to be $0.5h$–$2h$, h being the fluid velocity mesh size, from the consideration of both the stability and the accuracy. Our numerical experiments indicate that for relatively high Reynolds numbers (in the hundreds) the solid mesh size being smaller than the fluid one will always cause instability, whereas being larger than $2h$ might give rise to too much loss of accuracy, irrespective of the rigid body problems we studied before or the flexible body problems studied here, and therefore h_s being h–$2h$ is a good choice. For the rectangular solid mesh, the size in one direction can be slightly smaller than the fluid mesh size if the one in the other direction is larger than h.

One certainly does not have to use identical elements for the solid configuration and the Lagrange multiplier. For example, for a highly slender body, fine solid mesh (e.g. two layers of meshes across the body) may be still necessary for determining the solid deformation with acceptable accuracy, as indicated in our experiment below, while coarser Lagrange multiplier mesh (one layer of meshes) is better chosen to allow for a larger fluid mesh size. Nevertheless, the computational bottleneck of our algorithm lies in the solution of the solid sub-problem, since the fluid problem can be solved very efficiently with the fast solver. For a big solid system, the currently used direct solver is not practical, and has to be replaced with a iterative solver such as Bi-CGSTAB [37].

4. Numerical experiment

Two problems are considered here: one is the oscillation of an infinitely wide flexible plate along the flow direction, and the other is the self-sustained oscillation of a flexible plate across the flow direction.

4.1. Oscillation of a flexible plate along the flow direction

Fig. 2 shows the schematic diagram of the first test problem, which was introduced by Baaijens [15] and mimics the motion of heart-valve leaflets in a two-dimensional setting. The channel height is H and the leaflet is located midway in the streamwise direction. The homogeneous Dirichlet condition and the symmetry condition are imposed on Γ_2 and Γ_4, respectively. Since the velocities normal to the walls vanish, the homogeneous Neumann conditions for ϕ in (56) hold on Γ_2 and Γ_4, according to (58). In the original problem of Baaijens, flow flux conditions rather than velocity conditions are imposed on Γ_1 and Γ_3, which gives rise to a difficulty in applying the fast solver to (56). To circumvent this difficulty, we simply give parabolic velocities along Γ_1 and Γ_3 but move them to places far away from the leaflet to avoid the disturbance of the leaflet motion on the velocity profile. The mean velocity and the channel height H are taken as the characteristic velocity and length, respectively.

Corresponding to the dimensional parameter values in one example of Baaijens, the dimensionless ones are: $\rho_r = 1$, $\overline{G} = 10^3$, $Re = 100$ and $U = 1.5y(2-y)\sin(\frac{2\pi}{T}t)$ along Γ_1 and Γ_3, here, T being the dimensionless period for the flow flux changing with time and equal to 10. The length and thickness of the leaflet are 0.8 and 0.0212, respectively. The channel length is set to be 8, which, we found, produces the same results as the case of the channel length being 10. The motion of the leaflet and the corresponding flow fields are illustrated in Fig. 3, which are obtained with Scheme 2, the solid mesh (3×80), $h = 1/128$, $\Delta t = 0.005$ and $\overline{\lambda}_0 = 10^5$. For the time $t/T = 0$–0.25, the leaflet deflects to the right (Figs. 3(a) and (b)) as the flow rate increases. For $t/T = 0.25$–0.5, the leaflet tends to bounce back as the flow flux decreases (Figs. 3(c)–(e)). Subsequently, the reverse flow drives the leaflet to deflect to the left (Figs. 3(f)–(h)). The results are

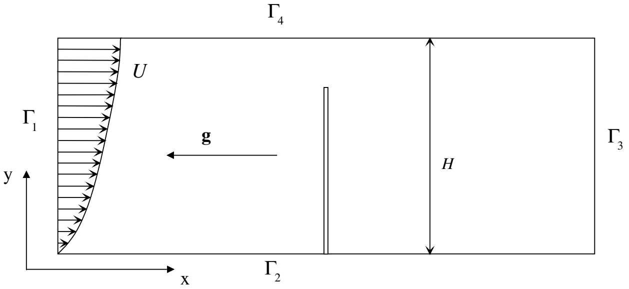

Fig. 2. Schematic diagram of the test problem: oscillation of a flexible plate along the flow direction.

qualitatively same as those obtained by Baaijens, however, our leaflet appears to be more deflected than Baaijens' (Fig. 7 in his paper), particularly at $t/T = 0.5$ (Fig. 3(e)). We will examine the effects of the numerical parameters including the mesh size, the time step and the penalty parameter on the accuracy of our results.

We found that Scheme 1 is not stable for the neutrally buoyant problem, but is robust for the non-neutrally buoyant case. The configurations of the leaflets at $t/T = 0.5$ and $\rho_r = 2$ and 5, respectively, are calculated with the two schemes and compared in Fig. 4. There are almost no differences between the results from the two schemes for both cases of $\rho_r = 2$ and 5, indicating that Scheme 2 is as accurate as Scheme 1 and there is no reason why its accuracy would degenerate for the neutrally buoyant case.

Fig. 5 plots the results of convergence tests for the penalty parameter $\overline{\lambda}_0$. We see that $\overline{\lambda}_0$ being two-order in magnitude larger than $\overline{G}$ can provide roughly converged solutions for the cases of $\overline{G} = 1000$ and particularly $\overline{G} = 500$. Therefore, this criterion for the choice of the value of $\overline{\lambda}_0$ is used for all other calculations in this work. In addition, Fig. 5 shows that the leaflet for $\overline{G} = 500$ can be much more deformed than the one for $\overline{G} = 1000$.

The results of convergence tests for the solid mesh and the time step are shown in Fig. 6. The fluid velocity mesh size h is fixed to be 1/128, which should be fine enough to produce a sufficiently accurate fluid flow solution. From Fig. 6, the convergence behavior of the scheme with the time step is good, since the results obtained from $\Delta t = 0.01$ and $\Delta t = 0.005$ are in good agreement, however, the convergence behavior with the solid mesh is relatively poor, which is the main source of numerical errors in our scheme. It is difficult to obtain a completely converged solution with the refinement of the solid mesh due to the fact that if we increase the number of meshes along the leaflet while fixing the number of meshes across the body, the computed leaflet always appears to be more deflected. Fortunately, the solution becomes less sensitive to the mesh aspect ratio with the increasing number of the transverse meshes and the tendency for the solutions to converge with the mesh refinement is clear. To elucidate whether this poor mesh convergence behavior is fully due to the drawback of the DLM/FD method, or partly because of the difficulty in the solution of the solid problem, we perform the mesh convergence tests for the solid sub-problem alone. For simplicity, we solve (47) with only the solid elastic term and the Lagrange multiplier term remained, and the Lagrange multiplier is set to be -1 homogeneously in the solid domain. The results are presented in Fig. 7, and we observe the same convergence behavior with the mesh aspect ratio as in the above fluid–solid interaction problem. Therefore, we owe the poor convergence performance with the solid mesh of our method mainly to the challenging solid problem itself, not the DLM/FD scheme.

From the convergence tendencies manifested in both Figs. 6 and 7, it seems that the optimal aspect ratio of the solid mesh is not unity but a value between 1 and 2. Hence, for both the accuracy and the stability, one better sets the solid mesh size in each direction to be between h and $2h$, and the size along the body is larger than the one in the other direction. The success of the use of three layers of meshes across the body

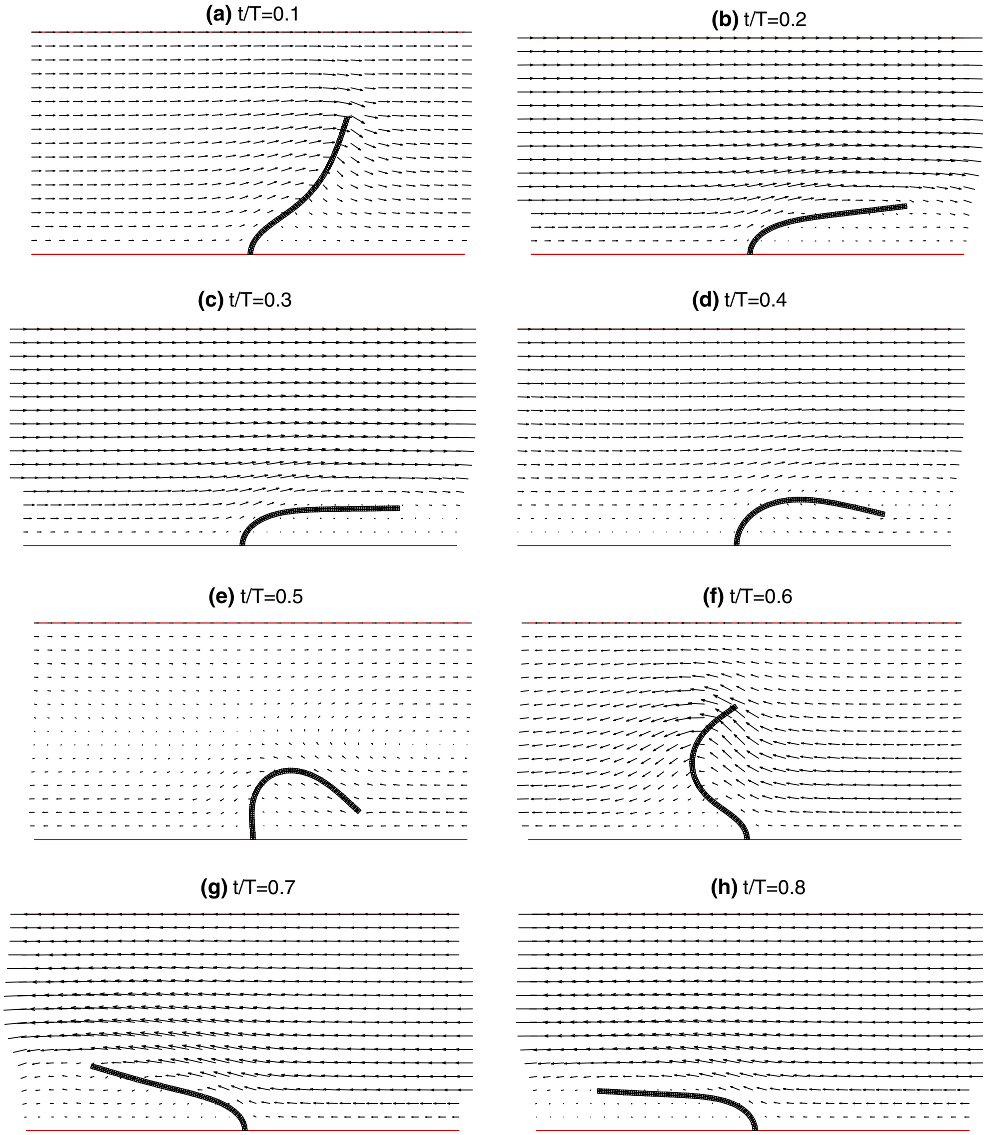

Fig. 3. The configurations of a neutrally buoyant infinitely wide plate (leaflet) and the flow fields at different times in a channel with the flow flux changing periodically. The results are obtained with Scheme 2, solid mesh (3 × 80), $h = 1/128$, $\Delta t = 0.005$, $\overline{G} = 10^3$, $Re = 100$ and $\bar{\lambda}_0 = 10^5$.

(3 × 60 and 3 × 80) in the present problem shows that the mesh size in one direction can be slightly smaller than the fluid mesh size ($\frac{0.0212}{3} < \frac{1}{128}$) if the one in the other direction is larger than h. The computation with the mesh 3 × 90 was observed not stable. Fig. 6 indicates that the results obtained with two layers of meshes across the body are acceptable if the above criterion is satisfied (2 × 54 and 2 × 60), considering the difficulty in determining the leaflet half top configuration accurately. The leaflet configuration of Baaijens at $t/T = 0.5$ is close to our 2 × 40 one, and it is possible that his results also suffered from the use of the large mesh aspect ratio, although his formulation and computational scheme are different from ours.

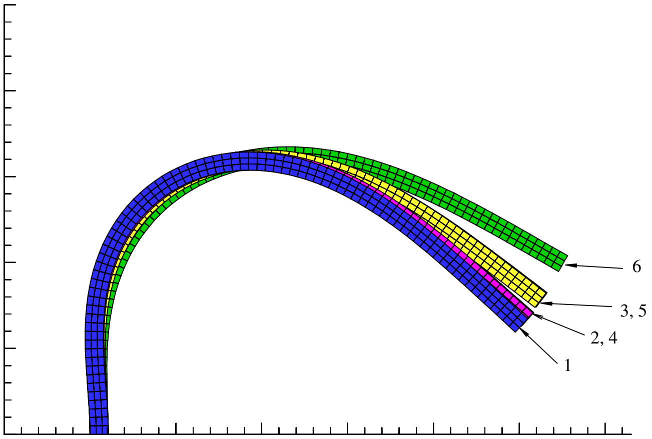

Fig. 4. The effect of the density ratio on the configurations of the leaflets at $t/T = 0.5$, and the comparisons between the results obtained from the two schemes. (1) $\rho_r = 1$, Scheme 2; (2) $\rho_r = 2$, Scheme 2; (3) $\rho_r = 5$, Scheme 2; (4) $\rho_r = 2$, Scheme 1; (5) $\rho_r = 5$, Scheme 1; (6) $\rho_r = 10$, Scheme 1. $Fr = 0$, $\overline{G} = 10^3$ and $Re = 100$ for all cases. The results from the two schemes are in excellent agreement with each other. The effect of the solid inertia is not very important for this streamwise oscillation problem.

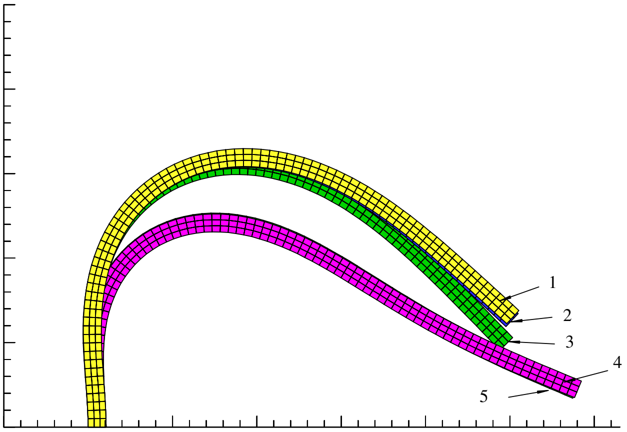

Fig. 5. Convergence tests for the penalty parameter $\bar{\lambda}_0$ using the configurations of the leaflets at $t/T = 0.5$. (1) $\bar{\lambda}_0 = 10^6$ and 10^7, respectively, and $\overline{G} = 10^3$; (2) $\bar{\lambda}_0 = 10^5$, $\overline{G} = 10^3$; (3) $\bar{\lambda}_0 = 10^4$, $\overline{G} = 10^3$; (4) $\bar{\lambda}_0 = 5 \times 10^4$, $\overline{G} = 5 \times 10^2$; (5) $\bar{\lambda}_0 = 5 \times 10^5$, $\overline{G} = 5 \times 10^2$. $\rho_r = 1$, $Re = 100$, mesh (3×80) and $\Delta t = 0.005$.

The effects of Fr on the configurations of the leaflets at $t/T = 0.5$ is shown in Fig. 8. We assume that gravity points in the negative x-direction, as shown in Fig. 2. For $\rho_r = 2$ and $Fr = 10$, the buoyant effect on the leaflet motion is significant. $Fr = 10$ may correspond to the case where the characteristic velocity (mean velocity) is 10 cm/s, the characteristic length (channel height) is 1 cm and the gravitational acceleration is 1000 cm/s^2. $\rho_r \neq 1$ introduces both the buoyant effect and the solid inertial effect, and for the present problem where the oscillation of the solid is driven by the periodical fluid flow, the solid inertial effect is relatively not important, as shown in Fig. 4. However, we will see that the solid inertia plays a crucial role in the self-sustained oscillation of a flexible plate swimming in a fluid. Fig. 8 also shows the effect of the Reynolds number, and we observe that the bouncing process of the leaflet is sensitive to Re when Re is between 100 and 200, but becomes less sensitive for $Re > 200$.

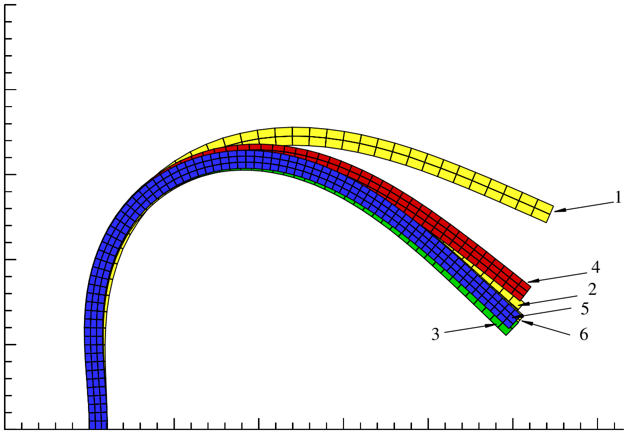

Fig. 6. Convergence tests for solid mesh and time step, using the configurations of the leaflets at $t/T = 0.5$. (1) Mesh (2×40), $\Delta t = 0.005$; (2) mesh (2×54, $\Delta t = 0.005$; (3) mesh (2×60), $\Delta t = 0.005$; (4) mesh (3×60), $\Delta t = 0.005$; (5) mesh (3×80), $\Delta t = 0.005$; (6) mesh (3×80), $\Delta t = 0.01$. $h = 1/128$, $\rho_r = 1$, $\overline{G} = 10^3$, $Re = 100$ and $\bar{\lambda}_0 = 10^5$. The convergence behavior of the scheme with time step is good, but relatively poor with solid mesh, which is mainly caused by the difficulty in solving accurately the solid problem alone.

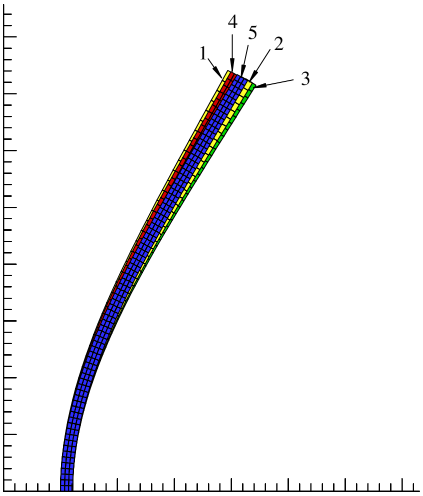

Fig. 7. Mesh convergence tests for the solid problem alone. The deformation of the leaflet is driven by a homogeneous body force that directs to the right and is unity in magnitude; the solid inertia and the flow are not considered. (1) Mesh (2×40); (2) mesh (2×54); (3) mesh (2×60); (4) mesh (3×60); (5) mesh (3×80). $\overline{G} = 10^3$, and $\bar{\lambda}_0 = 10^5$. The solution (leaflet top half configuration) is sensitive to the aspect ratio of the solid mesh, particularly for the coarser mesh, and the leaflet appears to be more flexible with the increasing number of the meshes along the leaflet for the same mesh resolution across the leaflet.

The effect of the fluid stress on the motion of the leaflet was found negligible for the case of $\rho_r = 1$, $\overline{G} = 10^3$, $Re = 100$ since the switch off this term did not cause any noticeable difference in the solid configuration.

4.2. Self-sustained oscillation of a flexible plate across the flow direction

The flow over a flexible plate in a channel is considered here. This problem is of great interest because it can be taken as a hydrodynamic model to probe the mechanisms in the practical flag-flapping and

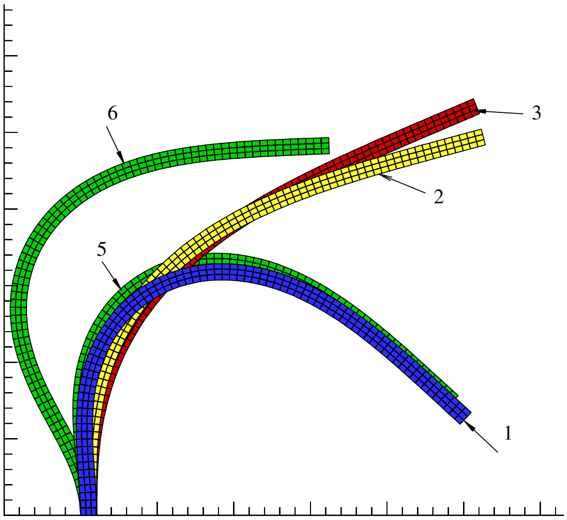

Fig. 8. The effects of *Re* and *Fr* on the configurations of the leaflets at $t/T = 0.5$. (1) $Re = 100$, $\rho_r = 1$; (2) $Re = 200$, $\rho_r = 1$; (3) $Re = 500$, $\rho_r = 1$; (4) $Re = 100$, $\rho_r = 2$, $Fr = 1$; (5) $Re = 100$, $\rho_r = 2$, $Fr = 10$. Gravity directs to the left.

fish-swimming problems. Zhang et al. [38] investigated experimentally the self-sustained oscillation of a filament in a flowing soap film, and observed an interesting so-called bi-stability phenomenon: in a certain range of the filament length, the filament can either be in a flapping state or a stretched-straight state, depending on the magnitude of the initial disturbance to the filament, and above a critical filament length, the stretch-straight state disappears and only the flapping state remains. The numerical studies on this problem have been attempted by Zhu and Peskin [29] and Farnell et al. [16]. Both groups of the authors used the fictitious-domain-based methods to solve the flow fields and the non-continuum-equation-based methods to track the motion of the filament, although, the two implementations are different. Zhu et al. [29] succeeded in reproducing the bi-stability phenomenon in their simulations. We aim to examine the effects of dimensionless control parameters on the motion of the flexible body in the present study, which have not been done in both previous works.

For our numerical model, the mainstream velocity is imposed on all boundaries of the channel, and one end surface of the plate is fixed at the channel center near the inlet, as shown in Fig. 9. We take the mainstream velocity U as the characteristic velocity and the length of plate L as the characteristic length. If we can neglect the effect of the channel length, then the dimensional parameter group consists of ρ_r, $\overline{G}$, Re, Fr, a_r and $\overline{H}$, here, a_r being the aspect ratio of the plate and $\overline{H}$ the dimensionless channel width. We assume that gravity points from the fixed end to the free end of the plate (to the right in Fig. 9). We consider only two cases for a_r: $a_r = 20$ and $a_r = 40$. We are not interested in the effect of $\overline{H}$, and its value is set to be 1 for $a_r = 40$ and 2 for $a_r = 20$ so that the ratio of the channel width to the plate thickness is fixed. The solid mesh 3×40 and $h = 1/64$ are used for $a_r = 20$, and mesh 3×80 and $h = 1/128$ for $a_r = 40$. For all cases, the dimensionless channel length is 8 and the time step is 0.005. The reference (or equilibrium) configuration of the plate (X, Y) is aligned with the streamwise direction, and the initial configuration (x_0, y_0) is declined with the streamwise direction by an angle $\tan^{-1}\delta_0$, i.e.:

$$\begin{aligned} x_0 &= X, \\ y_0 &= \delta_0 X + Y. \end{aligned} \tag{61}$$

It is clear that such a transformation conserves the area.

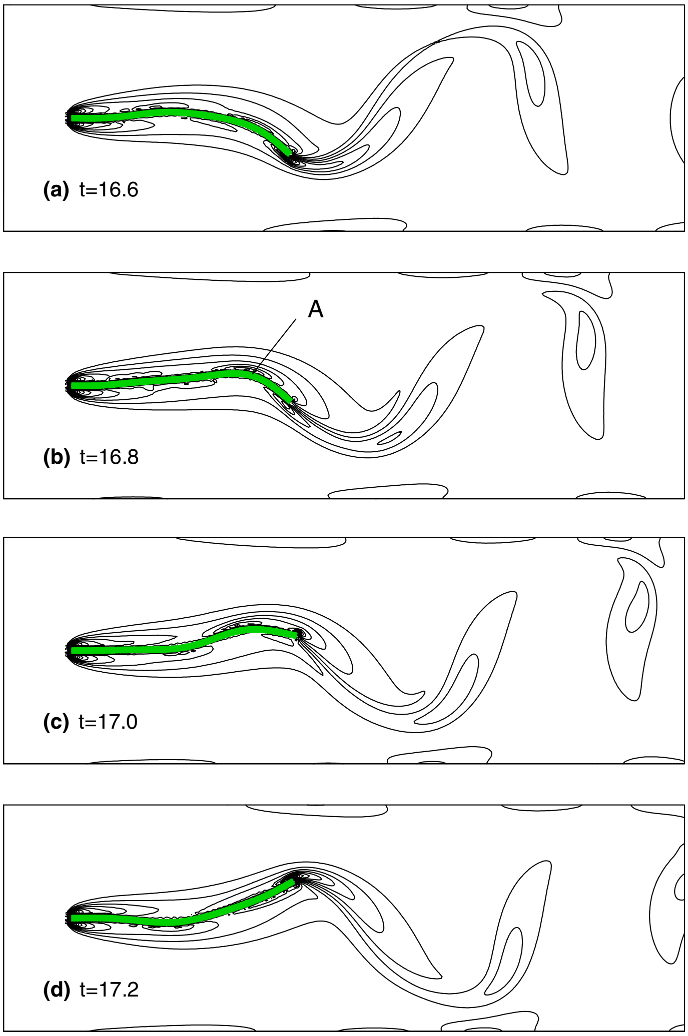

Fig. 9. The vorticity contours and the configurations of the plate at different times during around half a oscillatory period for $\delta_0 = 0.1$ and $(\rho_r, \overline{G}, Re, Fr, a_r, \overline{H}) = (8, 100, 500, 0, 40, 1)$. The vorticity increment for the contours is 5.0.

Fig. 9 shows the vorticity contours and the configurations of the plate at different times during around half a oscillatory period (the period is about 1.4) for $\delta_0 = 0.1$ and $(\rho_r, \overline{G}, Re, Fr, a_r, \overline{H}) = (8, 100, 500, 0, 40, 1)$. Similar to the flow over a stationary plate (see Fig. 16(a)), strong standing vortices always exist in the vicinity of the plate surface near the fixed end. The free end of the plate in Fig. 9(a) at $t = 16.6$ is near its trough. When the free end moves upwards, a convex top surface with a large curvature appears at $t = 16.8$ (i.e., around T/6 later) (marked by A in Fig. 9(b)) and the vorticity enhances there, which is similar to the flow over a blunt body. After $t = 17.0$, with the free end exceeding the rest parts of the plate, the vorticity begins to increase rapidly at the top end point, and a region of very concentrated vorticity forms at $t = 17.2$ when the free end almost reaches its peak (Figs. 9(c) and (d)). In our animations, the vortex appears to shed when the free end reaches the peak. The corresponding isobars are shown in Fig. 10, from which we see that the pressure differences across the plate act in such a way that they tend to straighten

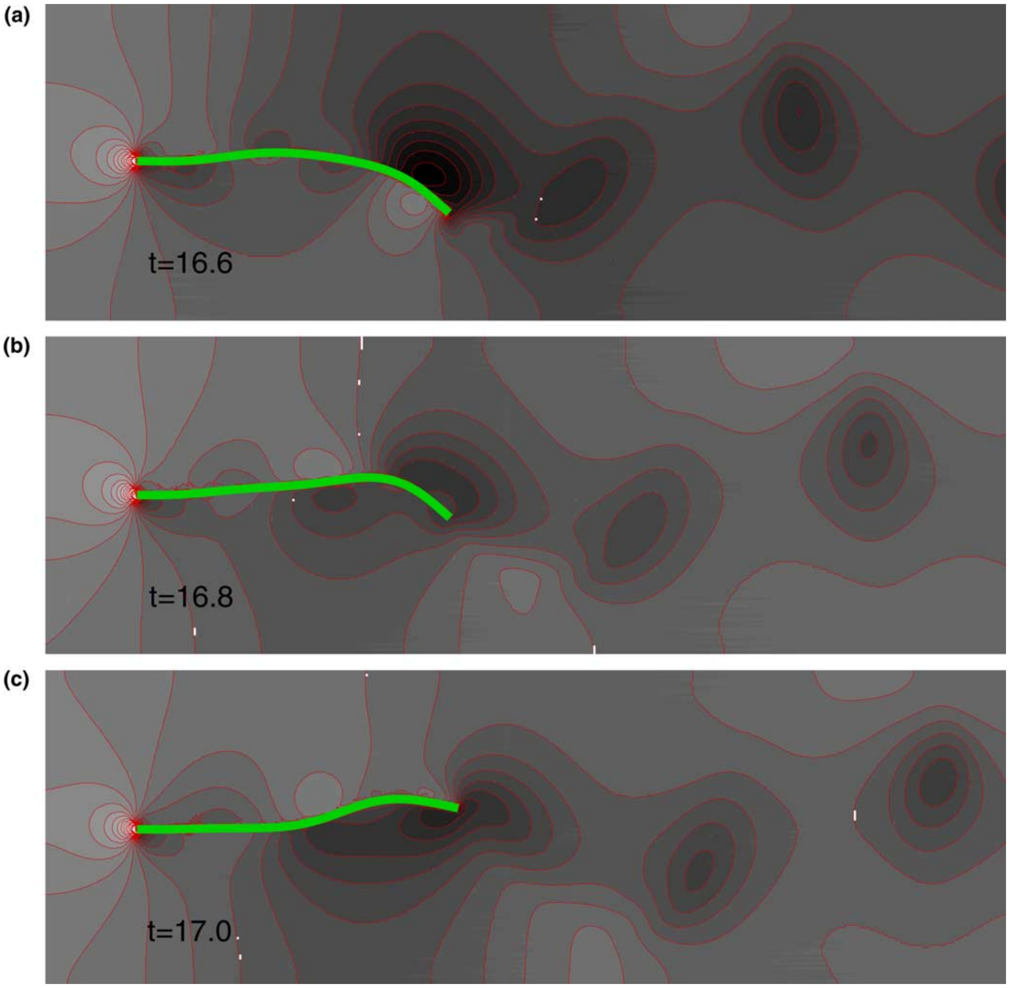

Fig. 10. The pressure contours and the configurations of the plate at different times during around half a oscillatory period for $\delta_0 = 0.1$ and $(\rho_r, \overline{G}, Re, Fr, a_r, \overline{H}) = (8, 100, 500, 0, 40, 1)$. The magnitude of the pressure is indicated by the gray scale, with the brightest area corresponding to the maximum pressure.

the plate of any specific configuration and make it align with the streamwise direction. For example, the free end parts at $t = 16.6$ and $t = 16.8$ are inclined with the streamwise direction, and then the pressure differences there help to push them upwards (Figs. 10(a) and (b)); the middle parts (a little closer to the free end) at $t = 16.8$ and $t = 17.0$ are moving upwards, and then the pressure differences there act to push them downwards (Figs. 10(b) and (c)). Since any parts of the plate (except the fixed point) oscillate sinusoidally with time (i.e., travelling wave, a phenomenon that was also observed in the experiment of Zhang et al. [38]), the pressure differences across the plate also change sinusoidally with time. Although, the pressure differences appear to straighten the configuration of the plate, they are expected to play an important role in the self-sustained oscillation of the plate due to the inertial motion and elastic response of the plate.

Figs. 11–14 show that one can turn a flapping state into a stretched-straight state by decreasing ρ_r or Re, or increasing $\overline{G}$ or Fr ($\rho_r \neq 1$) while keeping all other dimensionless parameters unchanged. Over the parameter range studied, the amplitude of the oscillation increases with increasing ρ_r (Fig. 11), or decreasing Fr

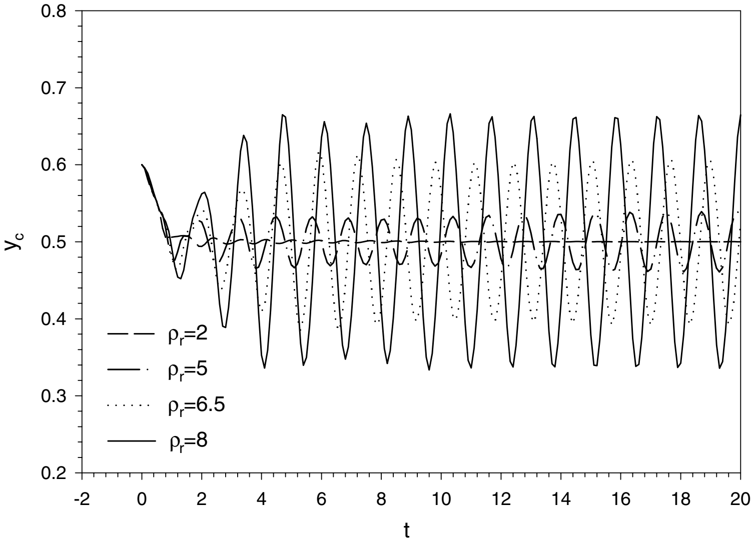

Fig. 11. The effects of ρ_r on the self-sustained oscillation of a flexible plate. y_c represents the y-coordinate of the center point on the plate free end surface. $\delta_0 = 0.1$ and $(\overline{G}, Re, Fr, a_r, \overline{H}) = (100, 500, 0, 40, 1)$.

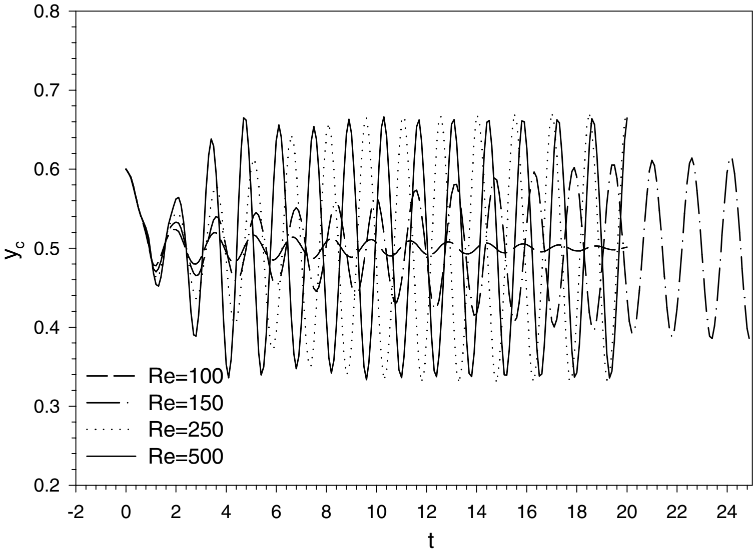

Fig. 12. The effects of Re on the self-sustained oscillation of a flexible plate. y_c represents the y-coordinate of the center point on the plate free end surface. $\delta_0 = 0.1$ and $(\rho_r, \overline{G}, Fr, a_r, \overline{H}) = (8, 100, 0, 40, 1)$.

(Fig. 13) or $\overline{G}$ (Fig. 14), whereas it decreases a little from $Re = 250$ to $Re = 500$ (Fig. 12). The dimensionless frequency (i.e., the Strouhal number St) increases with increasing Re (Fig. 12) or decreasing ρ_r (Fig. 11) obviously (though not significantly), or with increasing $\overline{G}$ (Fig. 14) or decreasing Fr (Fig. 13) very slightly. Zhu and Peskin [29] also observed a larger amplitude for a larger solid density and no-flapping for a neutrally buoyant plate in their simulations.

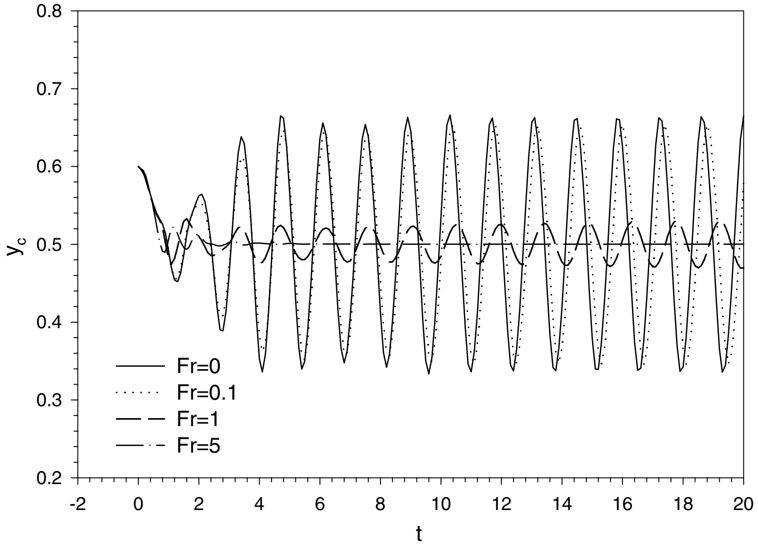

Fig. 13. The effects of *Fr* on the self-sustained oscillation of a flexible plate. y_c represents the *y*-coordinate of the center point on the plate free end surface. $\delta_0 = 0.1$ and $(\rho_r, \overline{G}, Re, a_r, \overline{H}) = (8, 100, 500, 40, 1)$.

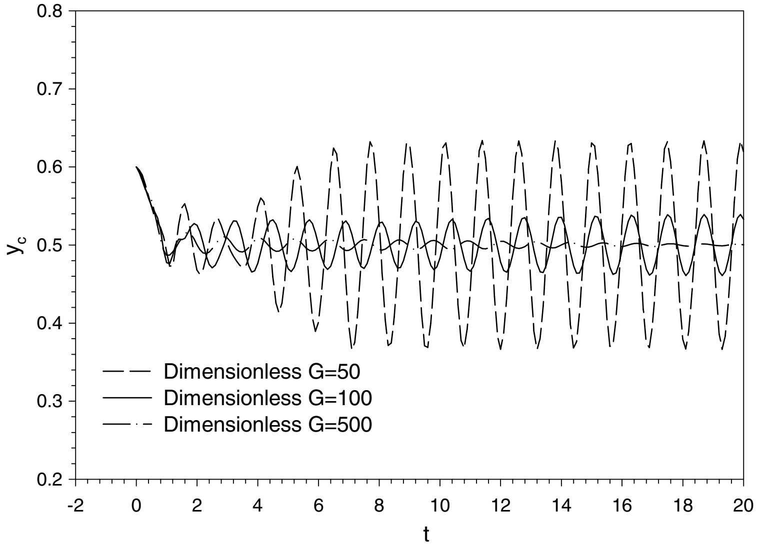

Fig. 14. The effects of $\overline{G}$ on the self-sustained oscillation of a flexible plate. y_c represents the *y*-coordinate of the center point on the plate free end surface. $\delta_0 = 0.1$ and $(\rho_r, Re, Fr, a_r, \overline{H}) = (8, 500, 40, 0, 1)$.

Fig. 15 shows the effects of the initial disturbance intensity δ_0 at $(\rho_r, \overline{G}, Re, Fr, a_r, \overline{H}) = (8, 100, 500, 0, 40, 1)$. We see that the plates will eventually flap with the same amplitude and frequency, irrespective of the initial disturbance intensity. For $\delta_0 = 0.001$, the plate appears to keep at rest for a long time, and it can be conceived that the rest state can remain even longer for a smaller δ_0, however, since the disturbance in an experimental laboratory can not be so small, we can say that the flapping state is the only stable

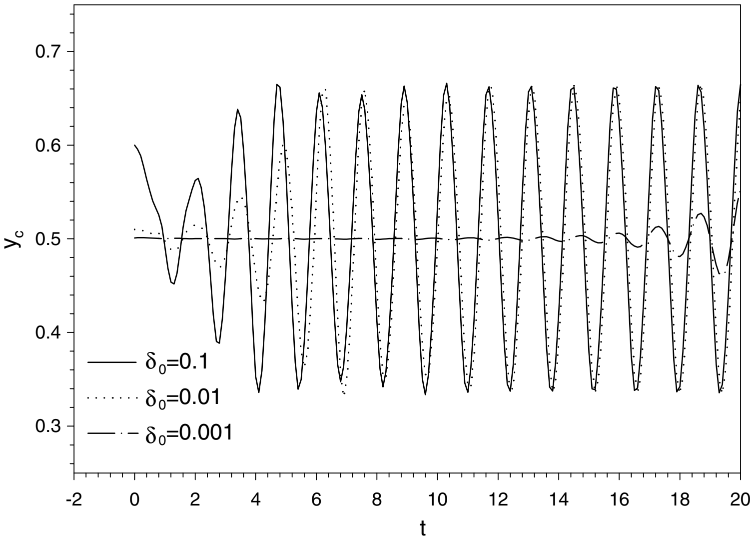

Fig. 15. The effects of the initial disturbance intensity on the self-sustained oscillation of a flexible plate. y_c represents the y-coordinate of the center point on the plate free end surface. $(\rho_r, \overline{G}, Re, Fr, a_r, \overline{H}) = (8, 100, 500, 0, 40, 1)$.

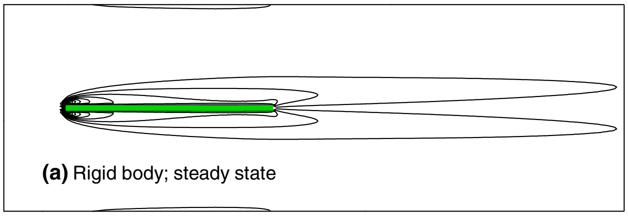

(a) Rigid body; steady state

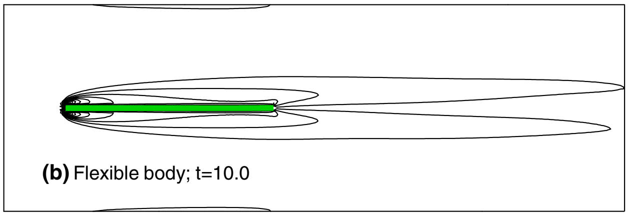

(b) Flexible body; t=10.0

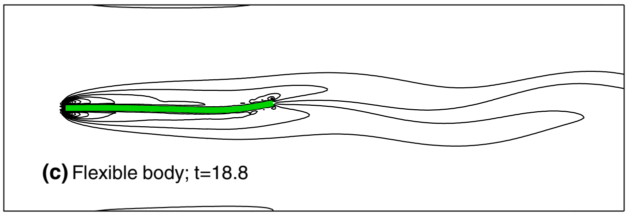

(c) Flexible body; t=18.8

Fig. 16. The vorticity contours and the configurations of the plate at (a) steady-state for the case of rigid-body, and (b) t = 10.0 and (c) t = 18.8 for the case of flexible-body at $\delta_0 = 0.001$ and $(\rho_r, \overline{G}, Re, Fr, a_r, \overline{H}) = (8, 100, 500, 0, 40, 1)$. The vorticity increment for the contours is 5.0.

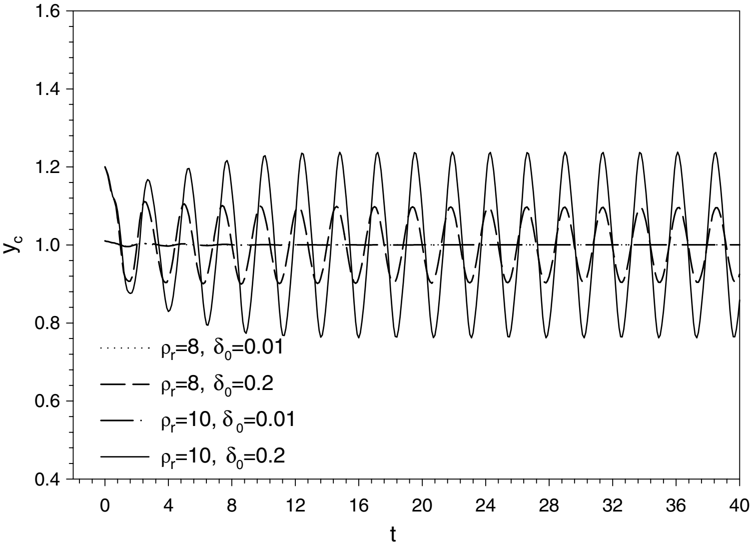

Fig. 17. Bi-stability phenomenon occurring at $a_r = 20$. y_c represents the y-coordinate of the center point on the plate free end surface. $(\overline{G}, Re, Fr, \overline{H}) = (100, 250, 0, 2)$.

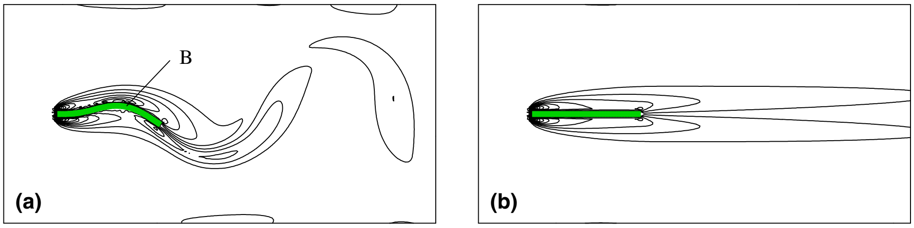

Fig. 18. The vorticity contours and the configurations of the plate for (a) $\delta_0 = 0.2$, showing that the plate is flapping, and (b) $\delta_0 = 0.01$, the plate remains at rest at the end of our simulation $t = 40$. $(\rho_r, \overline{G}, Re, Fr, a_r, \overline{H}) = (10, 100, 250, 0, 20, 2)$. The vorticity increment for the contours is 2.5.

state for this case. A close scrutiny at the motion of the plate reveals that the seemingly stationary plate is actually oscillating with a very small amplitude and with the same frequency as for the unsteady wake (Fig. 16(b)). By contrast, for a rigid body, the wake will become symmetrical and steady even if we initially impose an unsymmetrical flow about the centerline. Therefore, the instability in the flow over a flexible body a coupled instability between the flexible body and the flow, in the sense that the flow gives rise to the disturbances on the plate, and in turn the oscillation of the plate results in stronger unsymmetrical wakes (or even shedding of the vortices), as shown in Fig. 16.

Zhang et al. [38] observed that the increase in the dimensional filament length can lead a bi-stable state to a single flapping state. We consider case of $(\rho_r, \overline{G}, Re, Fr, a_r, \overline{H}) = (8, 100, 250, 0, 20, 2)$, which is resulted by shortening the plate dimensional length by half while keeping all other dimensional parameters unchanged in the above case. The system does exhibit two stable states: the plate for $\delta_0 = 0.2$ begins to flap after released, whereas the one for $\delta_0 = 0.01$ remains at rest during our simulation time (of course except the initial stage), as shown in Fig. 17. If we change $\rho_r = 8$ to $\rho_r = 10$, the same happens, and the visualization is shown in Fig. 18.

From Fig. 16(c), when the initial disturbance to the plate is very small, the amplification of the disturbances to the plate is mainly through the oscillation of the free end at early stage. If the free end of a plate is stable to small disturbances (this should be understood as the results of the response of the entire plate, not the free end alone, considering the role of the density ratio), and then the plate can remain its rest state, however, if the initial configuration disturbance is large, then the plate can extract sufficient energy from the flow to sustain its oscillation since the initial large deformation of the plate can produce strongly unsymmetrical fluid stress on the two sides of the plate (also from the vortex shedding), unlike the case of the stretched-straight state (as compared in Fig. 18). In the experiment of Zhang et al. [38], vortex shedding existed in the case of stretched-straight state, however, since the film was much thinner than the filament (film thickness: 3–4 μm and the diameter of the filament: 0.15 mm), the disturbance from the shedding of the Kármán-type vortices was still small (Gravity and surface tension may also help to stabilize the rest state in the experiments). The enormous geometrical difference between the experiment and our model precludes our attempt to make any quantitative comparisons. A comparison between Figs. 9(b) and 18(a) indicates that the most conspicuous bending part of the plate characterized by the convex surface (marked by A and B in the figures) is shifted closer to the fixed end for a smaller a_r. For $a_r = 20$ and $\rho_r = 8$, the position of the convex surface was found almost the same despite its much smaller flapping amplitude, compared to the case of $\rho_r = 10$. The tendency is consistent with the experimental observation that the flapping motion of a very long filament appeared to be limited to the free end region. Such a response of the plate with smaller a_r to the flow may be regarded as a reason why it is more difficult for the free end of a shorter stretched-straight plate to bend under small disturbances and then more difficult for a flapping instability to occur.

As the dimensional length of the plate is shortened, we find that both dimensionless amplitude and frequency of the flapping based on the plate length are reduced, from Figs. 11 and 17. The frequency is about 0.71 for $(\rho_r, \overline{G}, Re, Fr, a_r, \overline{H}) = (8, 100, 500, 0, 40, 1)$, and about 0.42 for $(\rho_r, \overline{G}, Re, Fr, a_r, \overline{H}) = (8, 100, 250, 0, 20, 2)$. The effect of the aspect ratio a_r on the frequency is much more significant than caused by any other parameters ρ_r, Re, $\overline{G}$ and Fr (Figs. 11–14); it can be reasonably assumed that the effect of $\overline{H}$ is insignificant for the present problems where the thickness of the plate is small compared to the channel width. Therefore, the characteristic dimensionless frequency of this self-sustained oscillation system should not be calculated using the length of the plate. If based on the thickness of the plate, the dimensionless frequency decreases from 0.021 ($\approx$0.41/20) for $a_r = 20$ to 0.018 ($\approx$0.71/40) for $a_r = 40$. We see that this frequency does not change much with the plate aspect ratio a_r or the plate dimensional length, which is in agreement with the experiments of Zhang et al. [38] where the initial decrease in the frequency was observed after the onset of the flapping instability and then the frequency largely remained unchanged, as the length of the filament was increased.

For both the fish-swimming problem and the self-sustained oscillation problem here, the flexible bodies transport travelling waves backward, however, there exists difference in the velocity of the travelling wave: for the fish-swimming case, the phase velocity is larger than the mainstream velocity, in contrast, for the current problem, we notice that the velocity of the wave is smaller than the mainstream velocity. Correspondingly, the thrust is produced and the reverse Kármán vortex street forms in the wake for the former case [39], and the drag (which can be inferred from Fig. 10) and the Kármán vortex street (Fig. 9) are observed for the problem here.

5. Conclusions

We have extended the distributed-Lagrange-multiplier/fictitious-domain (DLM/FD) formulation of Glowinski et al. [12] for the fluid/rigid-body interactions to deal with the fluid/flexible-body interactions by replacing Newton's equations of motion for the rigid body with the continuum equations for the general solid material. For our computational scheme, a first-order accurate fractional step scheme is employed to decouple the entire system into a fluid problem, a solid problem and a Lagrange multiplier problem, which simplifies the computation substantially; the flow problem is solved with the projection method on half-staggered grids; the solid problem is solved with the Lagrangian finite element method and the Newton iterative method; and the incompressibility of the material is implemented with the penalty function method.

The proposed method is applied to two typical fluid–structure interaction problems: the flow-driven oscillation of a flexible plate along the flow direction and the self-sustained oscillation across the flow direction. The first test problem shows that the accuracy of our method is acceptable, despite the relatively poor convergence behavior with the solid mesh, which is the main source of numerical errors in our scheme and however is mainly caused by the difficulty in solving the solid problem alone. For the second problem, we examine the effects of the dimensionless governing parameters on the flapping instability, and find that one can turn a flapping state into a stretched-straight state by decreasing the density ratio or the Reynolds number, or increasing the dimensionless shear modulus or the Froude number ($\rho_r \neq 1$) while keeping all other dimensionless parameters unchanged. Over the parameter range studied, the amplitude of the oscillation increases with increasing density ratio, or decreasing Froude number or shear modulus, whereas it is not sensitive to the Reynolds number once the instability takes place. The dimensionless frequency (i.e., the Strouhal number) increases with increasing Reynolds number or decreasing density ratio apparently (though not significantly), or with increasing shear modulus or decreasing Froude number very slightly. Our results confirm that the increase in the dimensional filament length alone can lead a bi-stable state to a single flapping state, while keeping the dimensional frequency of the oscillation largely constant. The most conspicuous bending part of the plate characterized by the convex surface with large curvature is shifted closer to the fixed end for a shorter plate, which could be responsible for the observation that a shorter plate is much more stable to small disturbances, allowing for the bi-stability phenomenon to take place. Different from the fish-swimming problem, the self-sustained oscillation problem here is characterized by the observations that the velocity of the backward travelling wave is smaller than the mainstream velocity and the Kármán vortex street forms in the wake.

Although, the method is implemented for the Newtonian fluid and the neo-Hookean elastic material in the two-dimensional case, the extensions to other fluids such as viscoelastic fluids (Yu et al. [24]), other solid materials and the three-dimensional case are straightforward.

Acknowledgments

The author thanks J.F. Brady and the Foundation for Fundamental Research on Matter (FOM) in the Netherlands for support of this research, Professor Yurun Fan, Professor Jorrit Mellema and Dr. Xing Shi for helpful discussions, and the anonymous referees of the paper for valuable suggestions that helped to improve the paper quality significantly.

References

[1] H.H. Hu, A. Patankar, M.Y. Zhu, Direct numerical simulations of fluid–solid systems using the arbitrary Lagrangian–Eulerian technique, J. Comput. Phys. 169 (2001) 427–462.

[2] A.A. Johnson, T.E. Tezduyar, 3D simulation of fluid-particle interactions with the number of particles reaching 100, Comput. Meth. Appl. Mech. Eng. 145 (1997) 301–321.

[3] J. Donea, S. Giuliani, J.P. Halleux, An arbitrairy Lagrangian–Eulerian finite element method for transient dynamic fluid–structure interactions, Compter Meth. Appl. Mech. Eng. 33 (1982) 689–723.

[4] C. Pozrikidis, Interfacial dynamics for stokes flow, J. Comput. Phys. 169 (2001) 250–301.

[5] T. Seta, K. Kono, S.Y. Chen, Lattice-Boltzmann method for two-phase flows, Int. J. Mod. Phys. B 17 (2003) 169–172.

[6] R. Scardovelli, S. Zaleski, Direct numerical simulation of free-surface and interfacial flow, Annu. Rev. Fluid Mech. 31 (1999) 567–603.

[7] J.A. Sethian, P. Smereka, Level set methods for fluid interfaces, Ann. Rev. Fluid Mech. 35 (2003) 341–372.

[8] G. Tryggvason, B. Bunner, A. Esmaeeli, D. Juric, N. Al-Rawahi, W. Tauber, J. Han, S. Nas, Y.-J. Jan, A Front-tracking method for the computations of multiphase flow, J. Comput. Phys. 169 (2001) 708–759.

[9] D.M. Anderson, G.B. McFadden, A.A. Wheeler, Diffuse-interface methods in fluid mechanics, Ann. Rev. Fluid Mech. 30 (1998) 139–165.
[10] T. Yabe, F. Xiao, T. Utsumi, The constrained interpolation profile (CIP) method for multiphase analysis, J. Comput. Phys. 169 (2001) 556–593.
[11] A.J.C. Ladd, R. Verberg, Lattice-Boltzmann simulations of particle–fluid suspensions, J. Stat. Phys. 104 (2001) 1191–1251.
[12] R. Glowinski, T.-W. Pan, T.I. Hesla, D.D. Joseph, A distributed Lagrange multiplier/fictitious domain method for particulate flows, Int. J. Multiphase Flow 25 (1999) 755–794.
[13] K. Hofler, S. Schwarzer, Navier–Stokes simulation with constraint forces: finite-difference method for particle-laden flows and complex geometries, Phys. Rev. E 61 (2000) 7146–7160.
[14] C.S. Peskin, Numerical analysis of blood flow in the heart, J. Comput. Phys. 25 (1977) 220–252.
[15] F.P.T. Baaijens, A fictitious domain/mortar element method for fluid–structure interaction, Int. J. Numer. Meth. Fluids 35 (2001) 743–761.
[16] D.J.J. Farnell, T. David, D.C. Barton, Numerical simulations of a filament in a flowing soap film, Int J. Numer. Meth. Fluids 44 (2004) 313–330.
[17] R. Glowinski, T.-W. Pan, J. Périaux, A fictitious domain method for Dirichlet problems and applications, Comput. Meth. Appl. Mech. Eng. 111 (1994) 283–303.
[18] R. Glowinski, T.-W. Pan, J. Périaux, A fictitious domain method for external incompressible viscous flow modeled by Navier–Stokes equations, Comput. Meth. Appl. Mech. Eng. 112 (1994) 133–148.
[19] R. Glowinski, T.-W. Pan, J. Périaux, A Lagrange multiplier/fictitious domain method for the Dirichlet problem. Generalization to some flow problems, Jpn. J. Ind. Appl. Math. 12 (1995) 87–108.
[20] R. Glowinski, T.-W. Pan, J. Périaux, A Lagrange multiplier/fictitious domain method for the numerical simulation of incompressible viscous flow around moving rigid bodies (I): the case where the rigid body motions are known a priori, C. R. Acad. Sci. Paris 324 (1997) 361–369.
[21] F. Bertrand, P.A. Tanguy, F. Thibault, A three-dimensional fictitious domain method for incompressible fluid flow problems, Int. J. Numer. Meth. Fluids 25 (1997) 719–736.
[22] P.A. Tanguy, F. Bertrand, R. Labie, E. Brito-De La Fuente, Numerical modelling of the mixing of viscoplastic slurries in a twin-blade planetary mixer, Trans. IChemE 74 (Part A) (1996) 499–504.
[23] R. Glowinski, T.-W. Pan, T.I. Hesla, D.D. Joseph, J. Periaux, A fictitious domain approach to the direct numerical simulation of incompressible viscous flow past moving rigid bodies: application to particulate flow, J. Comput. Phys. 169 (2001) 363–426.
[24] Z. Yu, N. Phan-Thien, Y. Fan, R.I. Tanner, Viscoelastic mobility problem of a system of particles, J. Non-Newtonian Fluid Mech. 104 (2002) 87–124.
[25] Z. Yu, N. Phan-Thien, R.I. Tanner, Dynamical simulation of sphere motion in a vertical tube, J. Fluid Mech. 518 (2004) 61–93.
[26] Z. Yu, Ph.D. Thesis, Dynamic simulation of particulate flows with the DLM method, University of Sydney, 2003.
[27] P. Le Tallec, J. Mouro, Fluid–structure interaction with large structural displacements, Comput. Meth. Appl. Mech. Eng. 190 (2001) 3039–3067.
[28] C.D. Eggleton, A.S. Popel, Large deformation of red blood cell ghosts in a simple shear flow, Phys. Fluids 10 (1998) 1834–1845.
[29] L. Zhu, C.S. Peskin, Simulation of a flapping flexible filament in a flowing soap film by the immersed boundary method, J. Comput. Phys. 179 (2002) 452–468.
[30] J. de Hart, G.W.M. Peters, P.J.G. Schreurs, F.P.T. Baaijens, A two-dimensional fluid–structure interaction model of the aortic value, J. Biomech. 33 (2000) 1079–1088.
[31] J. de Hart, G.W.M. Peters, P.J.G. Schreurs, F.P.T. Baaijens, A three-dimensional computational analysis of fluid–structure interaction in the aortic valve, J. Biomech. 36 (2003) 103–112.
[32] T. Belytschko, W.K. Liu, B. Moran, Nonlinear Finite Elements for Continua and Structures, Wiley, New York, 2000.
[33] V. Girault, P.-A. Raviart, Finite Element Methods for Navier–Stokes Equations: Theory and Algorithms, Springer-Verlag, Berlin, 1986.
[34] S. Armfield, R. Street, An analysis and comparison of the time accuracy of fractional-step methods for the Navier–Stokes equations on staggered grids, Int. J. Numer. Meth. Fluids 38 (2002) 255–282.
[35] D.W. Peaceman, H.H. Rachford, The numerical solution of parabolic and elliptic differential equations, J. Soc. Ind. Appl. Math. 3 (1955) 28–41.
[36] W.H. Press, S.A. Teukolsky, W.T. Vetterling, B.P. Flannery, Numerical Recipes in FORTRAN: the Art of Scientific Computing, Cambridge University Press, Cambridge, 1992.
[37] H.A. van der Vorst, Bi-CGSTAB: a fast and smoothly converging variant of Bi-CG for the solution of nonsymmetric linear systems, SIAM J. Sci. Stat. Comput. 13 (1992) 631–644.
[38] J. Zhang, S. Childress, A. Libchaber, M. Shelley, Flexible filaments in a flowing soap film as a model for one-dimensional flags in a two-dimensional wind, Nature 408 (2000) 835–839.
[39] G. Triantafyllou, M. Triantafyllou, D.K.P. Yue, Hydrodynamics of fish swimming, Annu. Rev. Fluid Mech. 32 (2000) 33–53.